Delayed induction of type I and III interferons mediates nasal epithelial cell permissiveness to SARS-CoV-2

Nasal interferon responses to SARS-CoV-2

Authors

Catherine F Hatton[1a], Rachel A Botting[2a], Maria Emilia Dueñas[2a], Iram J Haq[1,3a], Bernard Verdon[2a], Benjamin J Thompson[1], Jarmila Stremenova Spegarova[1], Florian Gothe[1,4], Emily Stephenson[2], Aaron I Gardner[1], Sandra Murphy[2], Jonathan Scott[1], James P Garnett[1], Sean Carrie[5], Jason Powell[1], C M Anjam Khan[2], Lei Huang[1], Rafiqul Hussain[6], Jonathan Coxhead[6], Tracey Davey[7], A John Simpson[1], Muzlifah Haniffa[2,8,9,10], Sophie Hambleton[1,11], Malcolm Brodlie[1,3b], Chris Ward[1b], Matthias Trost[2b], Gary Reynolds[2b], Christopher J A Duncan[1,12 b]*

[a] equal contribution

[b] equal contribution

* corresponding author: christopher.duncan@ncl.ac.uk

Affiliations

1. Translational and Clinical Research Institute, Faculty of Medical Sciences, Newcastle University, Newcastle upon Tyne, UK.

2. Biosciences Institute, Newcastle University, Newcastle upon Tyne, UK.

3. Paediatric Respiratory Medicine, Great North Children's Hospital, Newcastle upon Tyne Hospitals NHS Foundation Trust, Newcastle upon Tyne, UK.

4. Department of Pediatrics, Dr. von Hauner Children's Hospital, University Hospital, Ludwig-Maximilians-Universität Munich, Munich, Germany.

5. Population Health Sciences Institute, Newcastle University, Newcastle upon Tyne, UK.

6. Genomics Core Facility, Biosciences Institute, Newcastle University, Newcastle upon Tyne, UK.

7. Electron Microscopy Research Services, Newcastle University, Newcastle upon Tyne, UK.

8. NIHR Newcastle Biomedical Research Centre, Newcastle Hospitals NHS Foundation Trust, Newcastle upon Tyne, UK

9. Department of Dermatology, Newcastle Hospitals NHS Foundation Trust, Newcastle upon Tyne, UK

10. Wellcome Sanger Institute, Wellcome Genome Campus, Cambridge, UK

11. Great North Children's Hospital, Newcastle upon Tyne Hospitals NHS Foundation Trust, UK.

12. Department of Infection and Tropical Medicine, Newcastle upon Tyne Hospitals NHS Foundation Trust, UK.

Abstract

The nasal epithelium is a plausible entry point for SARS-CoV-2, a site of pathogenesis and transmission, and may initiate the host response to SARS-CoV-2. Antiviral interferon (IFN) responses are critical to outcome of SARS-CoV-2. Yet little is known about the interaction between SARS-CoV-2 and innate immunity in this tissue. Here we applied single-cell RNA sequencing and proteomics to a primary cell model of human nasal epithelium differentiated at air-liquid interface. SARS-CoV-2 demonstrated widespread tropism for nasal epithelial cell types. The host response was dominated by type I and III IFNs and interferon-stimulated gene products. This response was notably delayed in onset relative to viral gene expression and compared to other respiratory viruses. Nevertheless, once established, the paracrine IFN response began to impact on SARS-CoV-2 replication. When provided prior to infection, recombinant IFNβ or IFNλ1 induced an efficient antiviral state that potently restricted SARS-CoV-2 viral replication, preserving epithelial barrier integrity. These data suggest that the IFN-I/III response to SARS-CoV-2 initiates in the nasal airway and suggest nasal delivery of recombinant IFNs to be a potential chemoprophylactic strategy.

51 **INTRODUCTION**

52 SARS-CoV-2 is an emergent betacoronavirus responsible for coronavirus disease-19 (COVID-19)[1]. Since
53 its identification in late 2019, global pandemic transmission of SARS-CoV-2 has resulted in over 192
54 million confirmed infections and approximately 4.1 million deaths. SARS-CoV-2 infects target cells via
55 the entry receptor ACE2[2] leading to a spectrum of clinical outcomes, ranging from asymptomatic
56 infection to death[3]. Although multiple host factors (e.g. age, male sex, obesity) contribute to adverse
57 clinical outcome[4], the immune response also plays a decisive role, evidenced by the therapeutic
58 benefit of immunomodulatory agents including corticosteroids[5] or IL6 inhibition[6]. Yet much remains
59 to be understood about the immunopathogenesis of COVID-19. Identification of the cells hosting viral
60 entry and characterisation of their response to infection is essential to understanding pathogenesis
61 and improving therapy.

62 The nasal epithelium is believed to be a key entry point of SARS-CoV-2. Nasal epithelial tropism and
63 efficient viral shedding from the nasopharynx apparently contributes to the high transmissibility of
64 SARS-CoV-2[7], as well as to pathologic features such as anosmia[8]. As an early viral target cell, nasal
65 epithelial cells may also set the tone for the systemic immune response, potentially influencing disease
66 outcome[9]. These factors emphasise the need to study host-virus interaction in human nasal cells. *Ex*
67 *vivo* single-cell transcriptomic studies indicate that ciliated and/or goblet cells in the nasal mucosa
68 express *ACE2* and *TMPRSS2,* implicating them as probable SARS-CoV-2 target cells[10,11]. This has been
69 confirmed by *in vitro* and *in vivo* studies demonstrating SARS-CoV-2 infection of human nasal epithelial
70 cells[12-15]. Single-cell studies also revealed that nasal cells exhibit basal expression of an antiviral
71 expression programme, characterised by induction of several interferon-stimulated genes (ISGs),
72 suggesting that they may be primed to respond to viral infection[10,11]. Interestingly, *ACE2* is also
73 regulated by interferons (IFNs)[11,16], implying a complex relationship between IFN signalling and
74 tropism. Type I and type III IFN (IFN-I/III) systems play a critical role in human antiviral innate
75 immunity[17] and have been recently implicated in defence against SARS-CoV-2 susceptibility to severe
76 or life-threatening COVID-19 is associated with deleterious variants in *IFNAR* genes[18,19] and IFN-I

77 blocking autoantibodies[20]. *In vitro*, SARS-CoV-2 appears sensitive to the antiviral properties of IFN-I,
78 at least in cell lines[21,22], and this activity extends to *in vivo* model systems[9]. These findings motivate
79 studies to improve understanding of the interaction between SARS-CoV-2 and the IFN-I system in
80 primary human target cells, providing impetus to clinical trials of recombinant IFNs in treatment or
81 prophylaxis of COVID-19[23].
82 Organotypic cultures of primary human nasal epithelium differentiated at air-liquid interface (ALI) are
83 a translationally relevant primary cell model for studies of SARS-CoV-2 host-virus interaction[12], with
84 considerable potential to accelerate our understanding of pathogenesis. A small number of studies
85 using this model demonstrate that SARS-CoV-2 replicates efficiently in human nasal cells[12-14], yet
86 important questions concerning cellular tropism and their innate immune response remain
87 unresolved. Hou and colleagues report that only ciliated cells were permissive to SARS-CoV-2, despite
88 expression of ACE2 and TMPRSS2 by all cell types[13]. They hypothesised that post-entry factors, such
89 as innate immunity, might govern tropism. By contrast, Pizzorno and colleagues reported infection in
90 all major cell types (ciliated, secretory and basal cells)[14], consistent with prior indications from single-
91 cell RNA sequencing (scRNA-seq) data and studies in lower airway models[24,25]. While an IFN response
92 to SARS-CoV-2 can be detected in nasal cells[12,14], in apparent contrast to bronchial or alveolar
93 epithelial cells[26-28], the kinetics of induction and the antiviral function of IFNs in nasal epithelium has
94 not been systematically characterised.
95 Here we employed a comprehensive range of techniques, including scRNA-seq and proteomics, in
96 primary human nasal ALI cultures to define: (i) cellular tropism; (ii) the innate immune response to
97 SARS-CoV-2; and (iii) the antiviral activity of IFN-I/III. We observed broad cellular tropism of SARS-CoV-
98 2 for nasal epithelial cells, although secretory and ciliated cells were the most permissive. Nasal cells
99 mounted a delayed IFN response that began to exert control over viral replication at later times post-
100 infection. However, SARS-CoV-2 remained highly sensitive to IFN-restriction if exogenous IFN-I/III was
101 applied prior to infection. These data enrich our understanding of the interaction of SARS-CoV-2 and
102 the human IFN system at the earliest point of infection, with immediate therapeutic implications.

103

104 **RESULTS**

105 **SARS-CoV-2 robustly infects primary differentiated nasal epithelial cultures**

106 Primary nasal epithelial cultures were established from cryopreserved stocks from six adult donors,
107 obtained prior to the SARS-CoV-2 pandemic. Cells were expanded, differentiated and then matured
108 at ALI for 28 days, according to an established protocol[29]. We first sought to address their suitability
109 as a model of SARS-CoV-2 infection. Single-cell RNA-seq libraries were generated from two
110 representative donors, yielding 28,346 individual transcriptomes for analysis following quality control
111 (Fig. S1, Table S1). Following dimensionality reduction and Leiden clustering, eight populations were
112 discerned by their expression of established marker genes[11,30] (Fig. 1A, supplementary dataset 1). This
113 annotation was further validated using Seurat label transfer from a published scRNA-seq dataset from
114 nasopharyngeal swabs[15] (Fig. 1B). The major populations identified were ciliated, secretory, goblet
115 and basal cells, alongside two rarer populations of FOXN4+ deuterosomal cells[31] and ionocytes. Cells
116 expressed characteristic markers (Fig. 1C and supplementary dataset 1), corresponding closely to *ex*
117 *vivo* single-cell data from nasal brusings[15] (Fig. 1B). Immunostaining verified the presence of major cell
118 types in these cultures using well-established protein markers[13] - including acetylated alpha-tubulin-
119 positive (AAT) ciliated cells, mucin 5B-positive (MUC5B) secretory cells, mucin 5AC (MUC5AC)-positive
120 goblet cells, and tumour protein 63-positive (TP63) basal cells (Fig. S2) - with ciliated cells the most
121 abundant cell population. Consistent with published scRNA-seq data[10,11,15], mRNA for key SARS-CoV-2
122 entry receptors, *ACE2* and *TMPRSS2*, was expressed, albeit at relatively low levels, alongside other
123 genes implicated in SARS-CoV-2 entry such as *FURIN* and *CTSL* (Fig. S3)[32]. Robust expression of ACE2
124 and TMPRSS2 at the protein level was confirmed by immunoblotting of whole-cell lysates prepared
125 from mature ALI cultures (Fig. 1D). To establish their permissiveness to infection, nasal ALI cultures
126 were inoculated at the apical surface with a clinical SARS-CoV-2 isolate (BetaCoV/England/2/20) at an
127 approximate multiplicity of infection (MOI) 0.1 - consistent with other studies (0.1-0.5)[12-14] - and
128 monitored for infection over the next 72 h. Expression of SARS-CoV-2 *nucleocapsid (N)* gene and spike

129 (S) protein increased significantly over time, indicative of viral replication (Fig. 1E-F). This was
130 accompanied by the release of infectious viral particles, as determined by plaque assay of apical
131 washes on vero E6 cells, confirming productive infection (Fig. 1G). SARS-CoV-2 replication was
132 accompanied by a progressive decline in epithelial barrier integrity starting from 48 hours post-
133 infection (hpi), reflecting virus-induced epithelial dysfunction and/or potential cytopathic effect (Fig.
134 1H). These data established the suitability of the human nasal ALI system for modelling SARS-CoV-2
135 infection.
136

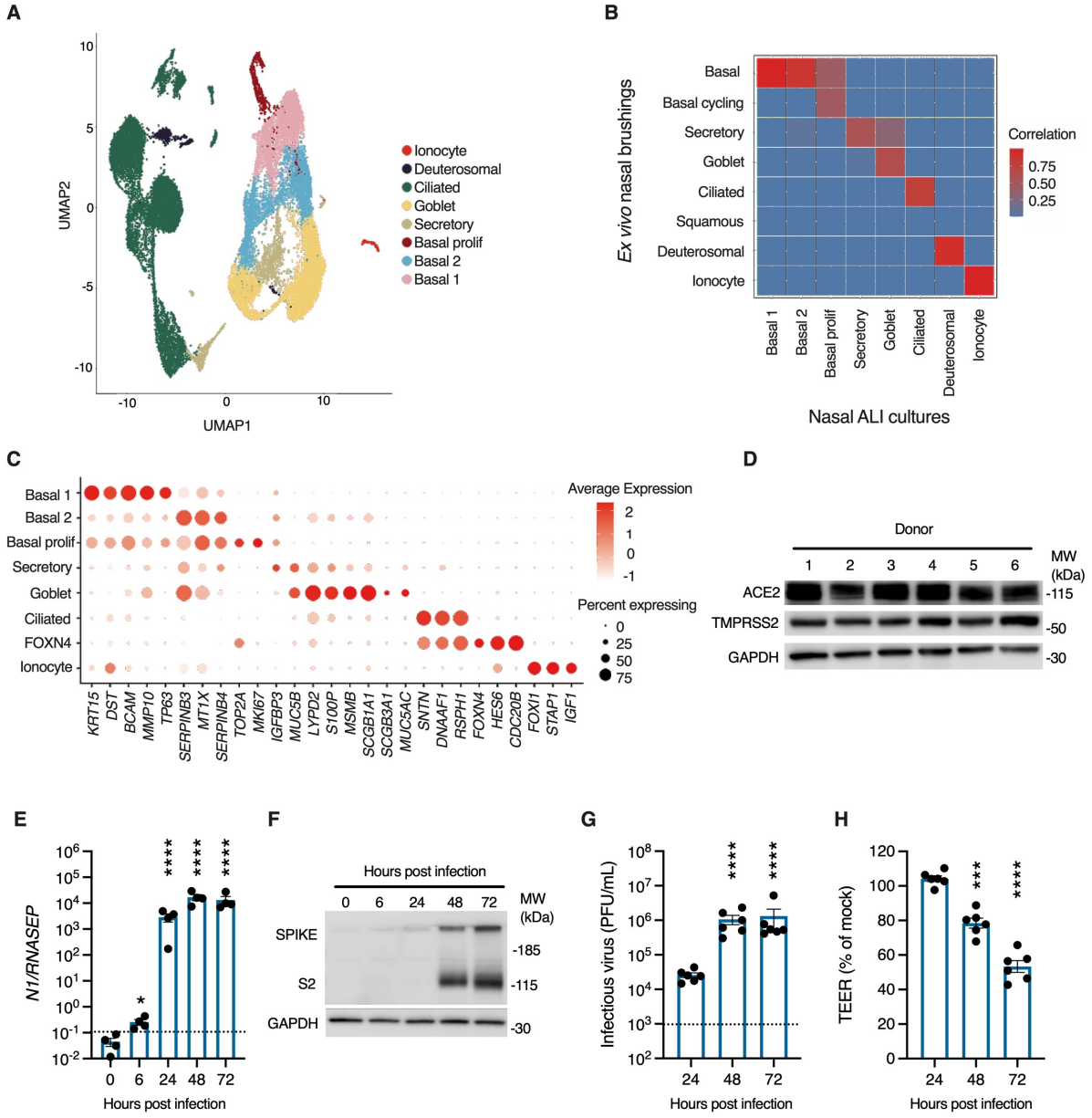

137

138 **Figure 1**. **Robust SARS-CoV-2 infection in a primary differentiated nasal epithelial ALI culture model.**
139 (A) UMAP visualisation of scRNA-seq data from nasal ALI cultures (28,346 single-cell transcriptomes
140 from two representative donors) revealed six major cell types. (B) Correlation between the annotation
141 from an external dataset of nasopharyngeal swabs and the assigned annotation of our scRNA-seq from
142 nasal ALI culture following label transfer. (C) Dot plot demonstrating expression of key markers
143 distinguishing cell types in annotated clusters, with intensity demonstrated by colour and size of the
144 dot representing the proportion of cells expressing the marker. (D) Immunoblot demonstrating ACE2
145 and TMPRSS2 expression by donor, representative of n=3 experiments. Nasal ALI cultures were
146 infected with SARS-CoV-2 (MOI 0.1) and subjected to various modalities to analyse infection. Whole-
147 cell lysates were prepared at the indicated times for RT-PCR analysis of expression of (E) SARS-CoV-2
148 nucleocapsid (*N*) gene expression normalised to the housekeeper *RNASEP2* (average of n=2 repeat
149 experiments in n=4 donors, mean ± SEM; * $P < 0.05$, **** $P < 0.0001$, ANOVA with Dunnett's post-test
150 correction compared to 0h). (F) Whole-cell lysates were prepared at the indicated times for
151 immunoblot analysis of expression of SARS-CoV-2 spike (S) and cleaved S2 protein expression
152 (representative of repeat experiments in n=4 donors). (G) Release of infectious viral particles was
153 determined by plaque assay of apical washings on permissive vero E6 cells (average of repeat
154 experiments in n=6 donors, mean ± SEM; **** $P < 0.0001$, ANOVA with Dunnett's post-test correction
155 compared to 24h). Dotted line represents lower limit of detection. (H) Transepithelial resistance
156 (TEER) measurements upon infection (expressed as % of mock-infected wells, n=6 donors, mean ±
157 SEM; *** $P < 0.001$, **** $P < 0.0001$, ANOVA with Dunnett's post-test correction compared to 24h).
158
159
160 **Evidence of broad cellular tropism of SARS-CoV-2**
161 To revisit the question of whether individual cell types are more or less permissive to SARS-CoV-2[13,14],
162 we first examined viral gene expression by scRNA-seq analysis at 24 hpi, selected to represent an early
163 stage in the progress of infection. While all cell types expressed viral transcripts, there were notable

differences both in the proportion of cells infected, and the relative abundance of different viral transcripts within these cells (Fig. 2A). Based on differential gene expression analysis between cell types (Wilcoxon rank sum test, one vs rest, $P < 0.05$), secretory and ciliated cells expressed higher levels of viral transcripts than other cell types, with viral transcripts most abundant in secretory cells (Fig. 2A, supplementary dataset 2). Deuterosomal cells also expressed abundant viral transcripts but were a rare population within these cultures, possibly limiting the power of this analysis. Basal cells are also located away from the apical surface; physical inaccessibility to apically-applied virus at this time point might at least partially account for this observation. To investigate tropism further, we undertook immunofluorescence analysis of viral spike (S) protein expression at 48 hpi (Fig. 2C-D, see Fig. S4 for background spike immunoreactivity in uninfected cells). This analysis revealed broadly similar proportions of ciliated, secretory and basal cells expressing S protein, with significantly lower spike immunoreactivity in MUC5AC positive (goblet) cells (Fig. 2D). However, the mean pixel intensity of S protein was significantly greater in ciliated cells than in other cell types, and significantly increased in secretory cells compared to basal cells (Fig. 2D). To corroborate these findings, we undertook analysis of intracellular virion-like structures (VLSs) at 48 hpi by transmission electron microscopy (TEM, Fig 2E), focusing on ciliated and secretory/goblet cells (the latter cell types were grouped for analysis as they could not be reliably distinguished based on morphology). Intracellular VLSs were observed in both ciliated and secretory/goblet cells, predominantly towards the apical surface (Fig. 2E). Consistent with immunofluorescence analysis of S protein intensity, there was a significant increase in the number of VLSs per cell in ciliated compared with secretory/goblet cells (Fig. 2E). Collectively, these data suggested that the virus is capable of entering, and replicating in, all major nasal cell types, but with quantitative differences in efficiency.

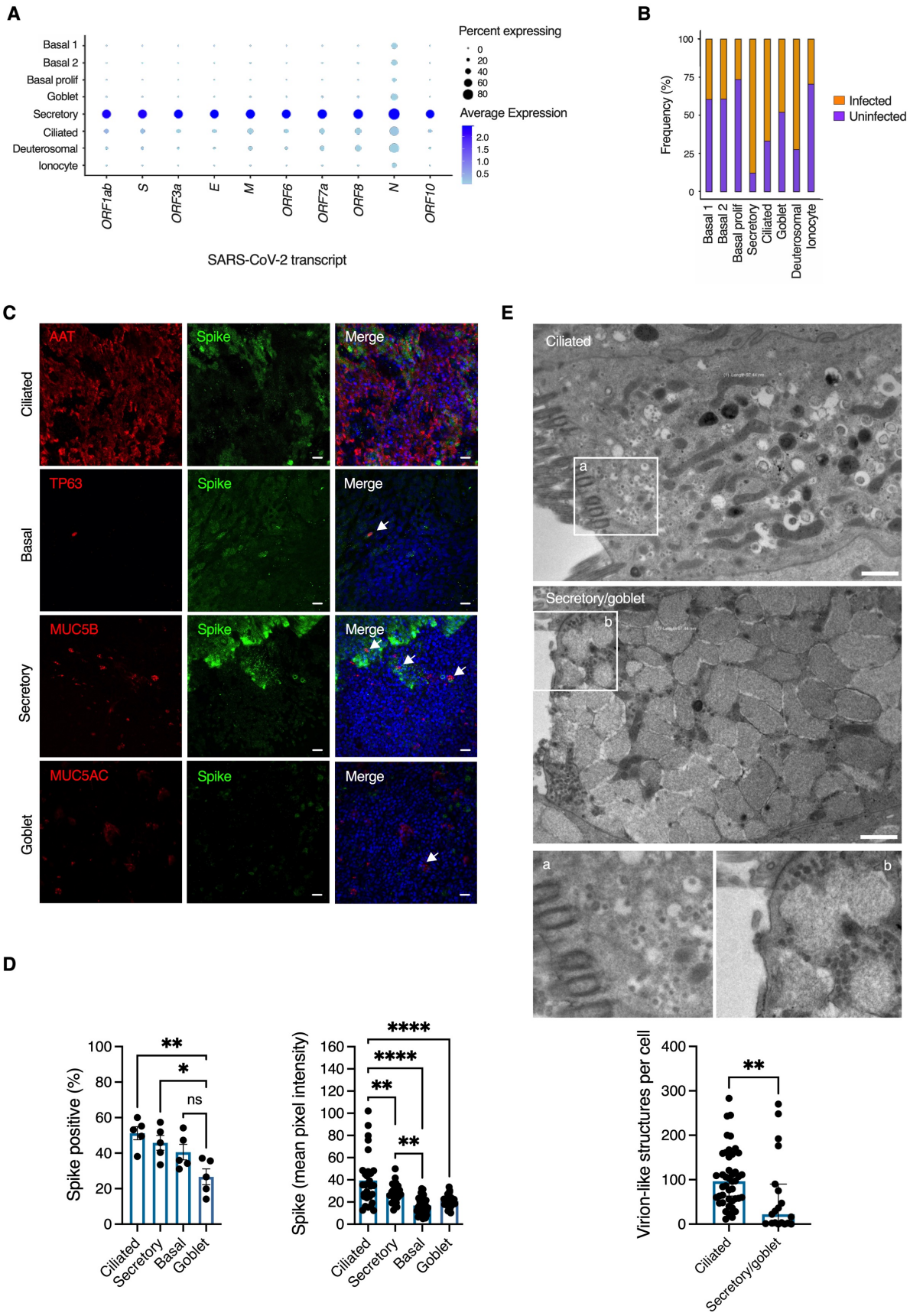
A
Basal 1
Basal 2
Basal prolif
Goblet
Secretory
Ciliated
Deuterosomal
Ionocyte
ORF1ab
S
ORF3a
E
M
ORF6
ORF7a
ORF8
N
ORF10
SARS-CoV-2 transcript
Percent expressing
0
20
40
60
80
Average Expression
2.0
1.5
1.0
0.5
B
Frequency (%)
100
75
50
25
0
Infected
Uninfected
Basal 1
Basal 2
Basal prolif
Secretory
Ciliated
Goblet
Deuterosomal
Ionocyte
C
Ciliated
Basal
Secretory
Goblet
AAT
TP63
MUC5B
MUC5AC
Spike
Merge
E
Ciliated
Secretory/goblet
a
b
D
Spike positive (%)
Spike (mean pixel intensity)
Virion-like structures per cell
Ciliated
Secretory
Basal
Goblet
Secretory/goblet
**
*
ns
****

188 **Figure 2. Broad tropism of SARS-CoV-2 for nasal cells**. Nasal ALI cultures were infected with SARS-
189 CoV-2 (MOI 0.1) and analysed using different modalities to explore tropism. At 24 hours post-infection
190 (hpi), cell suspensions were prepared from two representative donors for single-cell RNA sequencing
191 (scRNA-seq) and 28,346 individual transcriptomes passing QC were analysed. (A) Dot plot of scRNA-
192 seq data showing magnitude (colour) and proportion (size) of cell types expressing viral transcripts. E
193 = envelope; M = matrix; N = nucleocapsid; S = spike. (B) Relative proportion of infected cell types based
194 on expression of any viral transcript. Separately, nasal ALI cultures were fixed at 48 hpi and subjected
195 to immunofluorescence analysis. (C) Expression of viral S protein expression in ciliated (AAT), basal
196 cells (TP63), secretory (MUC5B) and goblet (MUC5AC) cells (arrowed) shown in (C). Scale bars = 10 μm
197 (representative of experiments in n=5 donors). (D) Quantification of cell-type specific expression of
198 viral S protein and S protein intensity at 48 hpi (n=5 donors, mean ± SEM; * P < 0.05, ** P < 0.01, ***
199 P < 0.001, **** P < 0.0001, ns = non-significant, ANOVA with Sidak's post-test correction for multiple
200 comparisons, indicated by lines). (E) Nasal ALI cultures were infected as above, fixed at 48 hpi for
201 transmission electron micrograph (TEM) analysis of SARS-CoV-2 infected ciliated and secretory/goblet
202 cells. Inserts (a) and (b) display virion-like structures in ciliated and secretory/goblet cells respectively.
203 Scale bars = 1 μm. Image analysis was undertaken to quantify virion-like structures as displayed in the
204 bar plot (n=3 donors, mean ± SEM ** P = 0.003, Mann-Whitney test).
205
206
207 **Characterisation of individual nasal cell responses to SARS-CoV-2**
208 Published *ex vivo* single-cell transcriptomic analyses report that nasal cell types exhibit the basal
209 expression of an innate antiviral gene signature, in the absence of viral infection, characterised by
210 several IFN-stimulated genes (ISGs)[10,11]. This signature correlated with *ACE2* expression, suggesting
211 conditioned expression to reduce susceptibility. Based on these reports, we examined scRNA-seq data
212 to characterise the innate antiviral response of nasal cells to SARS-CoV-2 infection at 24 hpi. In
213 unexposed cells, ISG signature scores were generated using context-specific ISGs from a published

214 IFN-treated nasal cell dataset[11] and compared using the Wilcoxon rank sum test. Gene set scores
215 greater than zero suggested expression levels higher than background gene expression, and was the
216 case for basal 1, secretory, goblet cells and ionocytes (Fig. 3A). The basal ISG signature was highest in
217 secretory cells despite abundant expression of viral RNA in these cells upon exposure to SARS-CoV-2
218 (Fig. 2A-B), suggesting basal ISG expression may not be sufficient to protect against infection. Next we
219 distinguished cells in three experimental conditions: unexposed (mock-infected); SARS-CoV-2-
220 exposed but uninfected (these 'bystander' cells would theoretically be exposed to IFNs and other
221 paracrine signals, but not infected); and SARS-CoV-2-infected (as defined by detectable expression of
222 SARS-CoV-2 transcripts). We undertook differential expression (DE) analysis between mock and
223 bystander or infected cells, labelling ISGs derived from the same list of context-specific ISGs (Fig. 3B,
224 supplementary datasets S3-4). There was minimal transcriptional response to infection in bystander
225 cells, including the absence of ISG induction, suggesting a lack of substantial paracrine IFN signalling
226 at this timepoint in keeping with reports in other airway models[25,27,28]. Interestingly, *IFITM* genes (ISGs
227 which have been paradoxically implicated in SARS-CoV-2 entry[33]) were downregulated in some
228 bystander cell populations. There was also minimal evidence of ISG induction in SARS-CoV-2 infected
229 cells, especially secretory, deuterosomal and goblet cells (Fig. 3B). In secretory and ciliated several
230 ISGs relating to antigen processing or presentation were downregulated upon infection (Fig. 3B). Basal
231 cells expressed a modest number of ISGs upon infection, specifically genes of the *IFITM* family, *IFI27*
232 and *IFI6* and the negative regulator of IFN-I signalling, *ISG15.* Consistent with this finding, gene-set
233 enrichment analysis (GSEA) revealed upregulation of IFN alpha/gamma responses in infected basal
234 cell populations but not in other cell types (Fig. 3C). The transcriptional response of infected secretory
235 and ciliated cells was characterised by widespread downregulation of expression, which may reflect
236 viral co-optation of transcriptional machinery of host cells, but this effect was not uniform. In
237 agreement with previous reports[34,35], genes related to oxidative phosphorylation were prominent
238 amongst downregulated genes, as were antigen presentation pathways. Pathway analysis also
239 predicted upregulation of NF-KB signalling in basal, secretory, goblet and ciliated cells, consistent with

240 previous findings[27,36]. Using DoRoTHea to explore regulon activity in these populations revealed higher
241 predicted *NFKB2* activity but limited evidence of widespread activation of IFN-mediated signalling (Fig.
242 S5). Transcripts for IFN-I (*IFNB, IFNK, IFNA5)* and IFN-III (*IFNL1)* were not significantly differentially
243 expressed and were detectable in only a small minority (~ 0.4%) of infected secretory cells (Fig. S6).
244 Whilst potentially consistent with the lack of paracrine signalling at this timepoint, this might also
245 reflect transient expression and/or insensitivity of detection by scRNA-seq; a similar pattern was
246 observed for other cytokines and chemokines (Fig. S6). Overall, this analysis showed that despite
247 evidence of NF-KB activation at 24 hpi, there was a minimal IFN response to SARS-CoV-2 in the cell
248 types with the highest levels of infection, consistent with previous reports in non-nasal epithelial
249 cells[25,27,28].
250

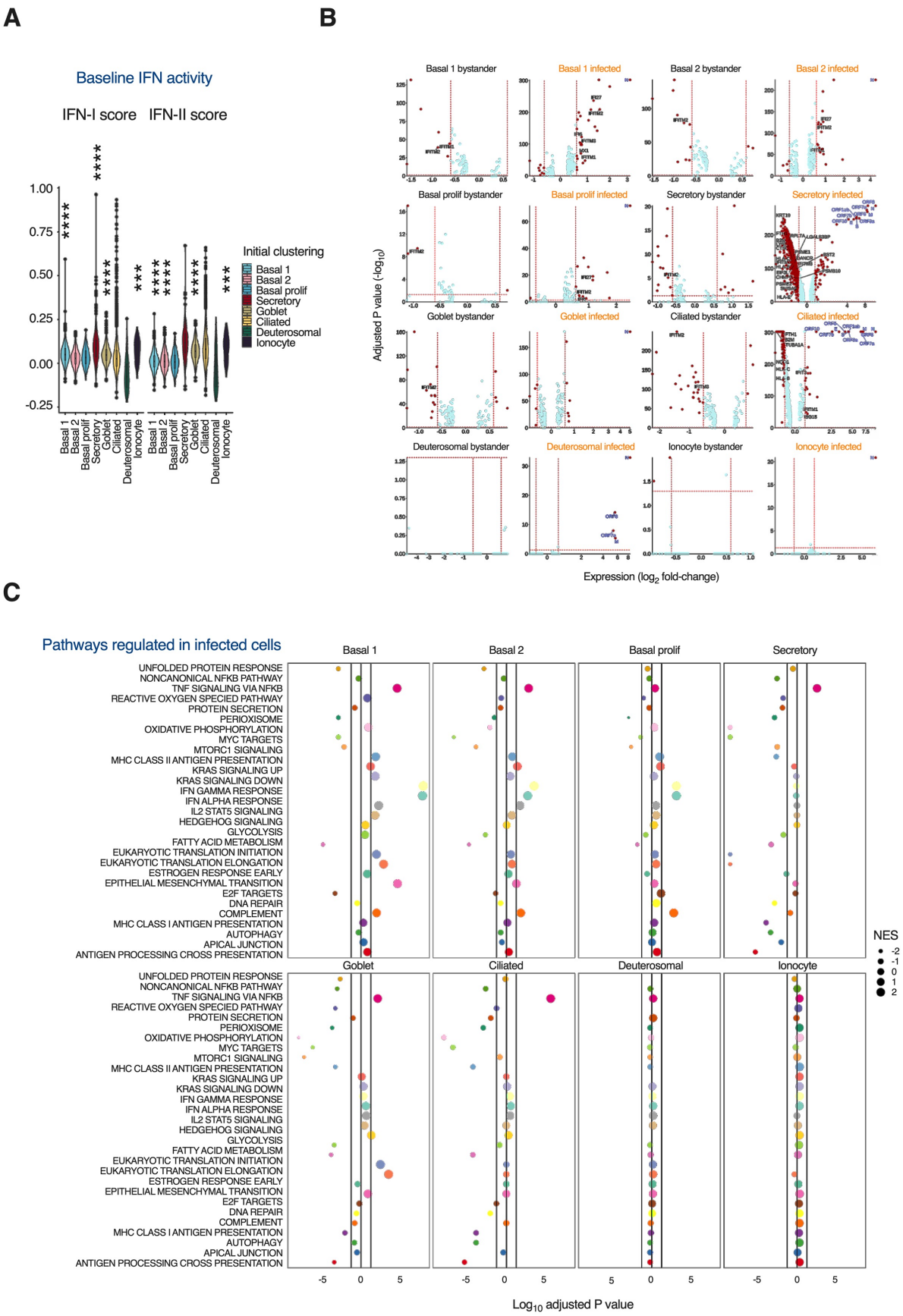
A
Baseline IFN activity
IFN-I score
IFN-II score
Initial clustering
Basal 1
Basal 2
Basal prolif
Secretory
Goblet
Ciliated
Deuterosomal
Ionocyte
B
Basal 1 bystander
Basal 1 infected
Basal 2 bystander
Basal 2 infected
Basal prolif bystander
Basal prolif infected
Secretory bystander
Secretory infected
Goblet bystander
Goblet infected
Ciliated bystander
Ciliated infected
Deuterosomal bystander
Deuterosomal infected
Ionocyte bystander
Ionocyte infected
Adjusted P value (-log10)
Expression (log2 fold-change)
C
Pathways regulated in infected cells
UNFOLDED PROTEIN RESPONSE
NONCANONICAL NFKB PATHWAY
TNF SIGNALING VIA NFKB
REACTIVE OXYGEN SPECIED PATHWAY
PROTEIN SECRETION
PERIOXISOME
OXIDATIVE PHOSPHORYLATION
MYC TARGETS
MTORC1 SIGNALING
MHC CLASS II ANTIGEN PRESENTATION
KRAS SIGNALING UP
KRAS SIGNALING DOWN
IFN GAMMA RESPONSE
IFN ALPHA RESPONSE
IL2 STAT5 SIGNALING
HEDGEHOG SIGNALING
GLYCOLYSIS
FATTY ACID METABOLISM
EUKARYOTIC TRANSLATION INITIATION
EUKARYOTIC TRANSLATION ELONGATION
ESTROGEN RESPONSE EARLY
EPITHELIAL MESENCHYMAL TRANSITION
E2F TARGETS
DNA REPAIR
COMPLEMENT
MHC CLASS I ANTIGEN PRESENTATION
AUTOPHAGY
APICAL JUNCTION
ANTIGEN PROCESSING CROSS PRESENTATION
Basal 1
Basal 2
Basal prolif
Secretory
Goblet
Ciliated
Deuterosomal
Ionocyte
NES
Log10 adjusted P value

252 **Figure 3. Characterisation of individual nasal cell transcriptional responses to SARS-CoV-2.** Nasal ALI
253 cultures were infected with SARS-CoV-2 (MOI 0.1). At 24 hours post-infection (hpi), cell suspensions
254 were prepared from two representative donors for single-cell RNA sequencing (scRNA-seq) and
255 28,346 individual transcriptomes passing QC were analysed. (A) A composite interferon-stimulated
256 gene (ISG) signature score was defined based on a published nasal cell dataset from cells treated with
257 IFN alpha and IFN gamma. Gene set scores greater than zero suggest expression levels higher than
258 background gene expression. Wilcoxon rank sum testing was performed for each cell type vs all with
259 Benjamini-Hochberg correction (* $P < 0.05$, ** $P < 0.01$, *** $P < 0.001$ **** $P < 0.0001$). (B) Differential
260 expression (DE) analysis by Wilcoxon rank sum test was undertaken to compare mock-infected cell
261 transcriptomes with those from bystander cells (without detectable viral transcripts) and infected cells
262 (with detectable viral transcripts) from the virus-exposed cultures. Volcano plots were generated with
263 vertical lines marking -/+ 1.5 fold change cut-offs (note $\log_2$ scale) and the horizontal line marking an
264 adjusted P value cut-off of 0.05 (< 0.05 was considered statistically significant). Individual genes
265 coloured as non-significant (light blue) and significant (red). Labels indicate viral transcripts (dark blue)
266 and epithelial-cell specific ISGs (black). (C) Gene-set enrichment analysis was undertaken by ordering
267 genes by fold change difference between mock-infected and infected cells by cluster. Vertical lines
268 indicated adjusted P value cut-off of 0.05. NES = normalised enrichment score.
269
270
271 **Kinetics of innate IFN-I/IFN-IIIs response to SARS-CoV-2**
272 To investigate the kinetics of the IFN-I/III response, expression of IFN-I (*IFNA1* and *IFNB*) and IFN-III
273 (*IFNL1*) was examined by RT-PCR at 6, 24, 48 and 72 hpi at the same MOI (0.1) as previous experiments.
274 Induction of *IFNL1* and *IFNB* was low at 24 hpi, consistent with scRNA-seq findings, but increased
275 significantly by 48 and 72 hpi (Fig. 4A). *IFNA1* was not induced, as observed in our scRNA-seq data.
276 Compared to the timing of initiation of viral gene expression - which was detectable at 6 hpi and
277 approached its maximum level by 24 hpi (Fig. 1E) - the induction of IFNs appeared delayed, as

278 suggested by previous studies[12,14,36]. Infection was accompanied by progressive upregulation of
279 proinflammatory cytokines such as *IL6, IL1B* and *TNF*, consistent with initiation of an NF-KB-dependent
280 inflammatory response (Fig. 4B). To look for evidence of a paracrine response to IFN-I/III, we analysed
281 expression of the ISGs *RSAD2* and *USP18* by RT-PCR, as well as the expression of RSAD2, USP18, ISG15
282 and MX1 proteins by immunoblotting. There was an increase in ISG mRNA and protein expression at
283 later times following the onset of *IFN* gene expression (Fig. 4C-D), potentially suggestive of paracrine
284 JAK-STAT signalling. To explore early induction of IFNs in more detail, we compared the response to
285 SARS-CoV-2 with other RNA respiratory viruses, influenza A virus (IAV) and parainfluenza virus 3
286 (PIV3). In this experiment, significant induction of *IFNB* and *IFNL1* occurred in response to both PIV3
287 and IAV, but not SARS-CoV-2, at 24 hpi (Fig. S7), and was accompanied by upregulation of ISGs *USP18*
288 and *RSAD2*. Infection of cell lines at high MOI are reported to enhance the relatively inefficient IFN-I
289 induction to SARS-CoV-2[25]. To confirm that the attenuated production of *IFNL1* and *IFNB* at early times
290 was not dependent on MOI, we repeated SARS-CoV-2 infections at 20-fold higher MOI (2), alongside
291 IAV (Fig. 4E), or a preparation of Sendai virus (SeV) containing a high proportion of immunostimulatory
292 defective viral genomes[32] as a positive control (Fig. S8). At 6 hpi, a time point at which *IFNB* and *IFNL1*
293 were significantly induced by IAV, there was no detectable response to SARS-CoV-2 (Fig. 4E).
294 Compatible observations were made with SeV (Fig. S8). At 24 hpi, SARS-CoV-2 exposure led to no
295 detectable induction of *IFNB* and significantly less *IFNL1* than IAV (Fig. 4E). This differential response
296 was reflected in the robust expression of ISGs *RSAD2, USP18* and *ISG15* at 24 h post-inoculation with
297 IAV but not SARS-CoV-2 (Fig. 4F). These observations recapitulated our previous RT-PCR and scRNA-
298 seq data with a lower MOI, and are consistent with other reports[12,27,37]. Collectively, the results
299 indicate that nasal epithelial cells express IFN-I/IIIs during SARS-CoV-2 infection, but that the response
300 is delayed relative to viral replication.
301

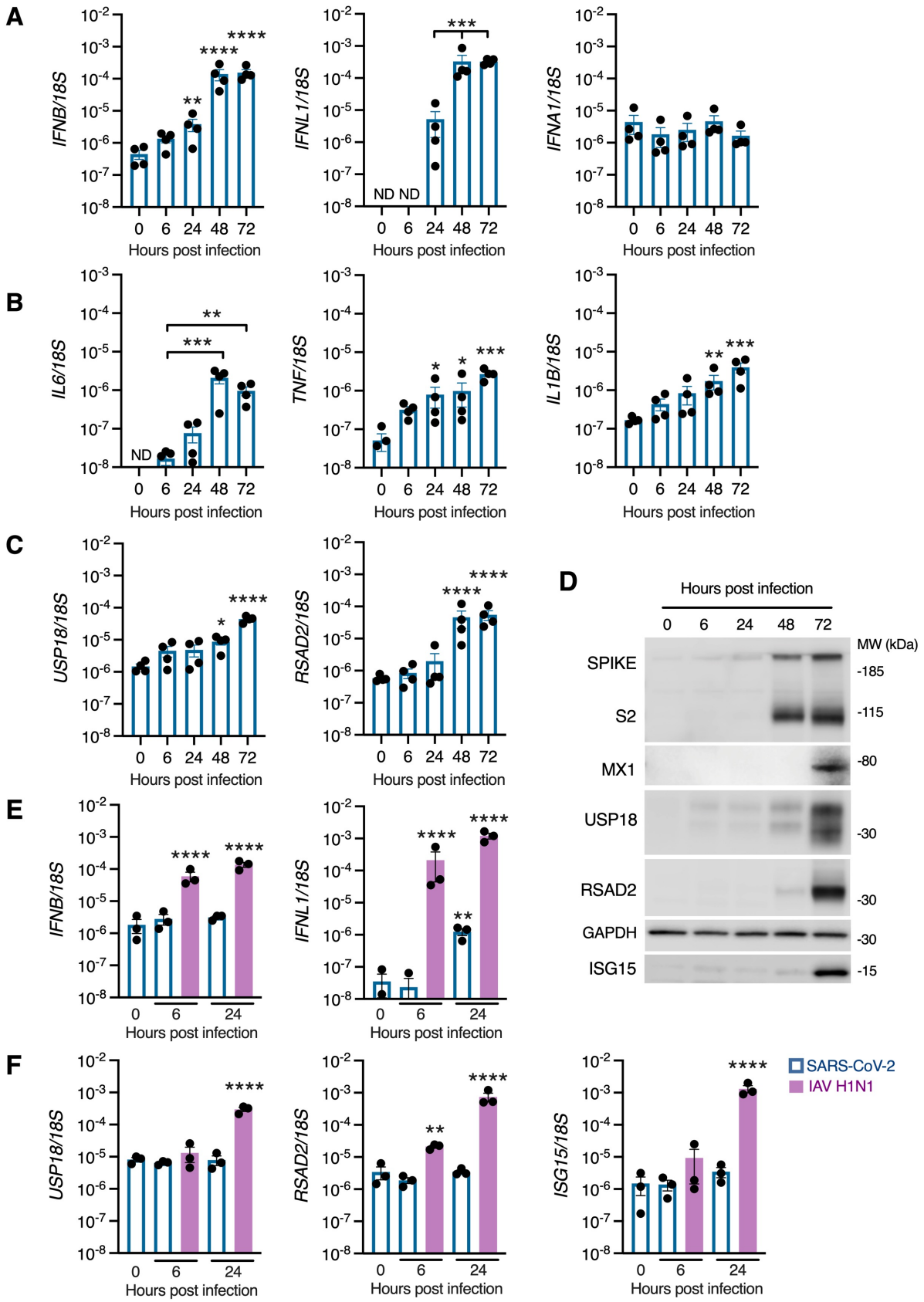

Figure 4. Delayed induction of IFN-I/III signalling in SARS-CoV-2-infected nasal ALI cultures. Nasal ALI cultures were infected with SARS-CoV-2 (MOI 0.1). Whole-cell lysates were prepared at the indicated

305 times for RT-PCR analysis of expression of (A) *IFNB*, *IFNL1* and *IFNA1* (B) *IL6*, *TNF* and *IL1B* and (C)
306 *USP18* and *RSAD2* (average of n=2 repeat experiments in n=4 donors, mean ± SEM; * P < 0.05, ** P <
307 0.01, *** P < 0.001 **** P < 0.0001, ANOVA with Dunnett's post-test correction compared to 6h [B,
308 *IL6*], 24h [A, *IFNL1*] or 0h [all others]). ND, Not detected. (D) Whole-cell lysates were prepared at the
309 indicated times for immunoblot analysis of S/S2, MX1, USP18, RSAD2 and ISG15 expression
310 (representative of experiments in n=4 donors). Nasal ALI cultures were infected with SARS-CoV-2 or
311 influenza A virus (IAV H1N1, purple bars) at MOI 2. Whole-cell lysates were prepared at the indicated
312 times for RT-PCR analysis of expression of (E) *IFNB*, *IFNL1* and (F) the ISGs *USP18*, *RSAD2* and *ISG15*
313 (n=3 donors, mean ± SEM; * P < 0.05, ** P < 0.01, *** P < 0.001 **** P < 0.0001, ANOVA with Dunnett's
314 post-test correction compared to 0h).
315
316
317 **IFN-signalling dominates the nasal host response to SARS-CoV-2 at the protein level**
318 To validate and extend these findings, we undertook an unbiased assessment of the host response to
319 SARS-CoV-2 infection by proteomics analysis. Whole-cell lysates were prepared from SARS-CoV-2 and
320 mock-infected nasal ALI cultures from six donors at 72 hpi. Lysates were analysed by quantitative mass
321 spectrometry (quality control data in Fig. S9). Overall, this analysis detected the differential expression
322 (DE) of 180 proteins including viral proteins such as S, M, N, ORF1AB, ORF3A and ORF8 (Fig. 5A
323 supplementary dataset S4). The most highly increased host protein was Sorting Nexin 33 (SNX33), an
324 endosomal protein that has not yet been implicated in the life cycle of SARS-CoV-2. Notably, other
325 SNX proteins (e.g. SNX17 and SNX2) are involved in viral trafficking[38,39]. Infected and uninfected cells
326 clustered together by principal component analysis (Fig. 5B). Inspection of the DE proteins confirmed
327 a robust host innate immune response, dominated by ISG products (Fig. 5A). Functional annotation
328 revealed an enrichment of antiviral response and especially IFN-I signalling pathways (Fig. 5C, Table
329 S2). These data are consistent with our earlier findings and contrary to prior reports in cell lines or
330 human bronchial/tracheal epithelial cultures, where a robust endogenous IFN-I/III response to SARS-

331 CoV-2 was not detected[26-28]. Key antiviral ISG proteins identified included IFIT1-3, MX1-2, and the OAS
332 cluster (OAS1-3), the latter associated with genetic susceptibility to severe COVID-19[19] (Fig. 5C).
333 Significantly downregulated pathways were also identified, including TRIF-dependent toll-like
334 receptor signalling, as well as RNA polymerase II transcription and endosomal transport (Table S3).
335 This implied viral subversion of critical host functions, including host gene transcription, protein
336 trafficking and viral sensing. Proteins involved in the maintenance of epithelial tight junctions were
337 also downregulated, consistent with the loss of barrier integrity observed in earlier experiments (Fig.
338 1H).
339

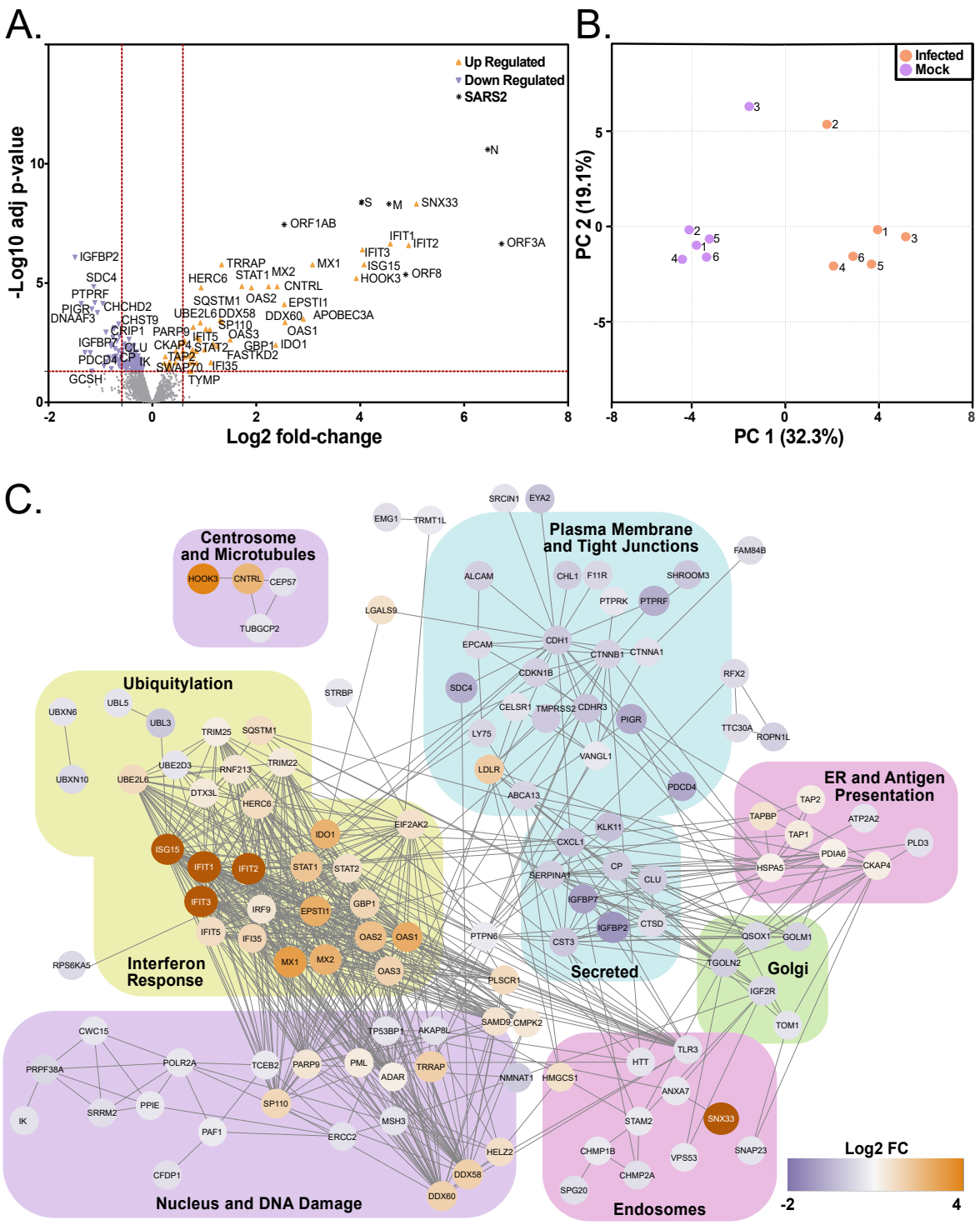

340

341 **Figure 5. An ISG response dominates the proteome of SARS-CoV-2 infected nasal ALI cultures.**

342 Differential proteomic profiling of SARS-CoV-2-infected nasal ALI cultures. Mass spectrometry-based

343 proteomics was carried out on whole-cell lysates prepared at 72 hpi (n=6 donors per condition). (A)

344 Volcano plot illustrating 180 differentially expressed proteins with increased (orange points) and

345 decreased (purple points) expression in infected as compared to mock-infected samples. Dotted red

346 lines indicate those proteins with a fold change of > 1.5 and adjusted p values <0.05. (B) Principal
347 component analysis of the whole proteome data set. (C) Functional annotation network of
348 differentially expressed proteins.
349
350
351 **Antiviral activity of IFN-I/III towards SARS-CoV-2 infection**
352 Given the prominence of the IFN-I/III response in the proteome of SARS-CoV-2-infected cells at later
353 times post-infection, a key question was whether this IFN-I/III response had any impact on SARS-CoV-
354 2 replication. To address this question, nasal ALI cultures were treated with the JAK inhibitor
355 ruxolitinib (RUX). RUX antagonises signalling downstream of IFNAR and IFNLR, owing to the
356 involvement of JAK1 in both signalling pathways. We reasoned that blocking paracrine IFN-I/III
357 signalling would reveal its impact, if any, on SARS-CoV-2 replication. Cells were treated with 10 µM
358 RUX (a dose optimised in prior experiments[40]) or vehicle control (DMSO) in the basal medium for 24
359 hours prior to infection. Nasal cultures were infected at the apical surface (MOI 0.1), inhibitors were
360 refreshed every 24h and infection was monitored up to 96 hpi. Lysates were prepared and analysed
361 by RT-PCR and immunoblot. RUX treatment abolished expression of ISGs *USP18, RSAD2 and ISG15* at
362 the mRNA and protein level (Fig. 6A-B), indicating that ISG induction was dependent on paracrine IFN-
363 I/III signalling, as previously suggested (Fig. 4D). By 96 hpi, approximately 24 hours after ISGs were
364 reliably detected at the protein level (Fig. 4D, Fig. 5A-C), blockade of this endogenous IFN response by
365 RUX led to a significant increase in both viral gene expression, assessed by RT-PCR (*N* gene) and
366 immunoblot (S/S2 protein, Figs 6B-D), and apical release of infectious virus measured by plaque assay
367 (Fig. 6E). These data provided further evidence that SARS-CoV-2 triggered an endogenous paracrine
368 IFN-I/III response in nasal cells, which once established began to impact SARS-CoV-2 replication.
369 An important follow-up question was whether nasal cells could mount an antiviral state to SARS-CoV-
370 2, providing IFN-I/III was delivered in a timely fashion. To address this, nasal ALI cultures were pre-
371 treated with exogenous IFNβ (1000 IU/mL) or IFNλ1 (100 ng/mL) for 16h to induce an antiviral state,

372 subsequently infected with SARS-CoV-2 at MOI 0.01 and examined at 48 hpi. Analysis of infection by
373 immunoblotting of whole-cell lysates for spike (S/S2) protein expression or plaque assay of apical
374 washes demonstrated a significant reduction in infection with either IFNβ or IFNλ1 pre-treatment (Fig.
375 7A-B). This was accompanied by robust induction of antiviral ISG products (Fig. 7A), and preservation
376 of barrier integrity (Fig. S10). It is worth noting that the ISG expression induced in response to
377 recombinant IFN-I/III at 48 hpi was substantially greater than that induced by endogenous IFN-I/III
378 production (Fig. 7A). Thus exogenous IFN-I/III was capable of inducing in the nasal epithelium an
379 antiviral state that potently inhibited SARS-CoV-2 infection, providing it was delivered (a) prior to
380 infection, and (b) at sufficient concentration. This IFN-sensitivity of SARS-CoV-2 contrasts with the
381 relative resistance of SARS-CoV[21]. These data suggest that mucosal delivery of IFNβ or IFNλ1 is a
382 potential therapeutic strategy for SARS-CoV-2. In clinical practice, IFNs are unlikely to be used prior to
383 infection, unless this is part of a prophylactic regimen. To determine the effectiveness of exogenously
384 applied IFNs once SARS-CoV-2 infection is underway, infected cells were treated with IFNβ or IFNλ1
385 at 6 or 24 hpi and examined for S/S2 protein expression by immunoblot (Fig. 7C-D) and release of
386 infectious virus by plaque assay (Fig. 7E). In this experiment, IFNβ and IFNλ1 treatment at 6 hpi
387 continued to impact on SARS-CoV-2 infection, whereas addition after 24 hpi had minimal effect.
388 Interestingly, ISG induction was still observed in response to IFN treatment at 24 hpi, albeit at reduced
389 magnitude in the case of IFNβ (Fig. 7C-D). These data suggest that SARS-CoV-2 may impair, but does
390 not abolish, JAK-STAT signalling in infected cells, implying that recombinant IFNs may have a
391 therapeutic role in established SARS-CoV-2 infection, as recently shown in animal models[9] and in early
392 phase clinical trials[41].
393

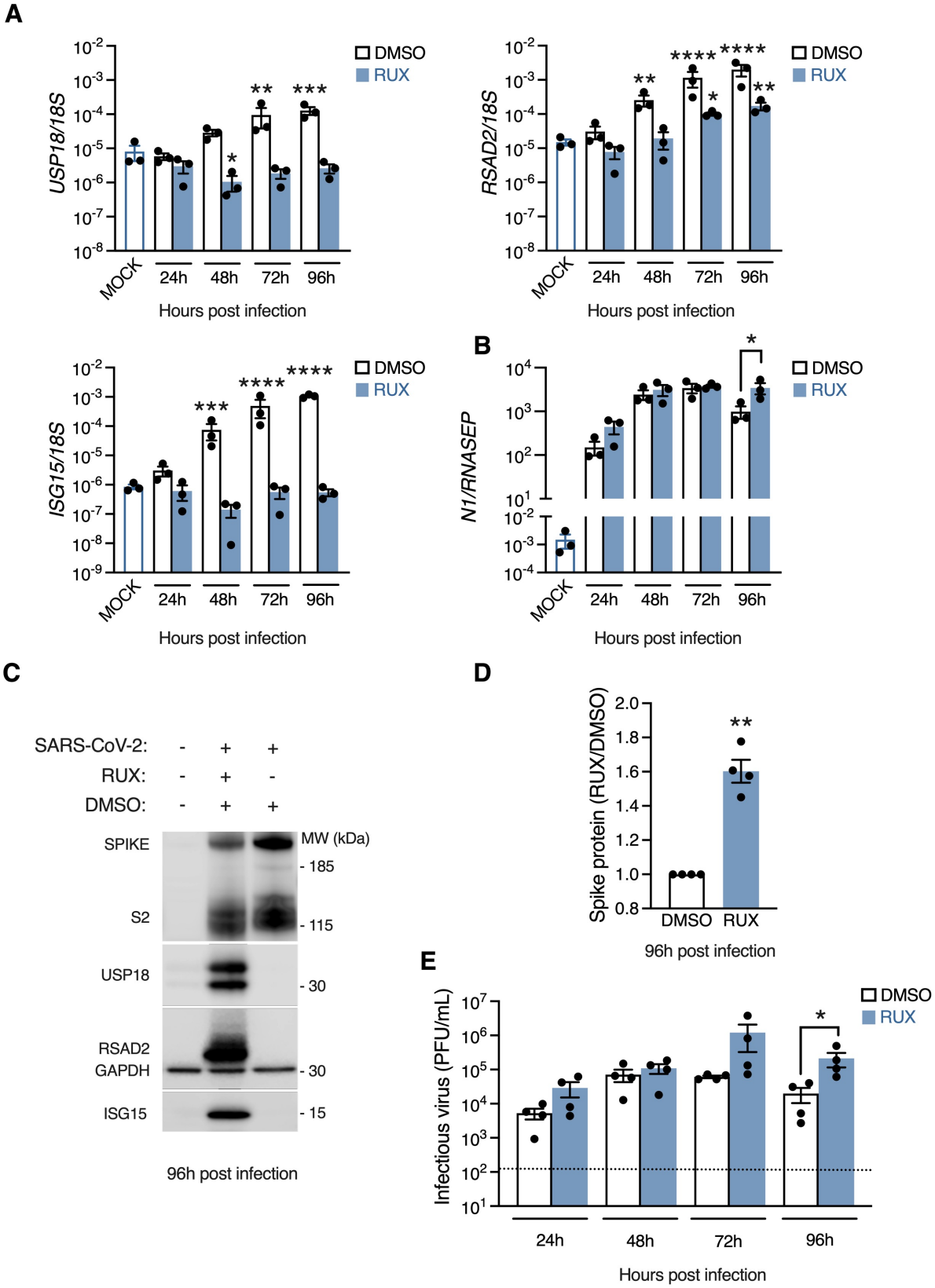

Figure 6. Impact of endogenous IFN-I/III signalling on SARS-CoV-2 infection. Nasal ALI cultures treated with ruxolitinib (RUX, 10 µM) or DMSO vehicle for 24 h prior to infection (MOI 0.1). Whole-

397 cell lysates were prepared at the indicated times for RT-PCR analysis of expression of (A) the ISGs
398 *USP18, RSAD2* and *ISG15* (n=3 donors, mean ± SEM; *** P < 0.001, **** P < 0.0001, ANOVA with
399 Dunnett's post-test correction compared to mock-infected cells) or (B) viral *N* mRNA (n=3 donors,
400 mean ± SEM; * P = 0.035 ANOVA with Sidak's post-test correction compared to DMSO control). (C)
401 Whole-cell lysates were prepared at 96 hpi for immunoblot analysis of viral S/S2 protein and host
402 RSAD2, USP18 and ISG15 protein expression (representative blot shown of experiments in n=4
403 donors). (D) Densitometry analysis of S+S2 protein intensity relative to GAPDH, normalised to the
404 DMSO control (data from C, n=4 donors, mean ± SEM; ** P = 0.003, one-sample t test). (E) Plaque
405 assay of apical washes collected at the times indicated showing a significant increase in infectious
406 particle release at 96 hpi (same experimental conditions as C-D; n=4 donors, mean ± SEM; * P = 0.015,
407 ANOVA with Sidak's post-test correction compared to DMSO control). Dotted line indicates lower limit
408 of assay detection.
409

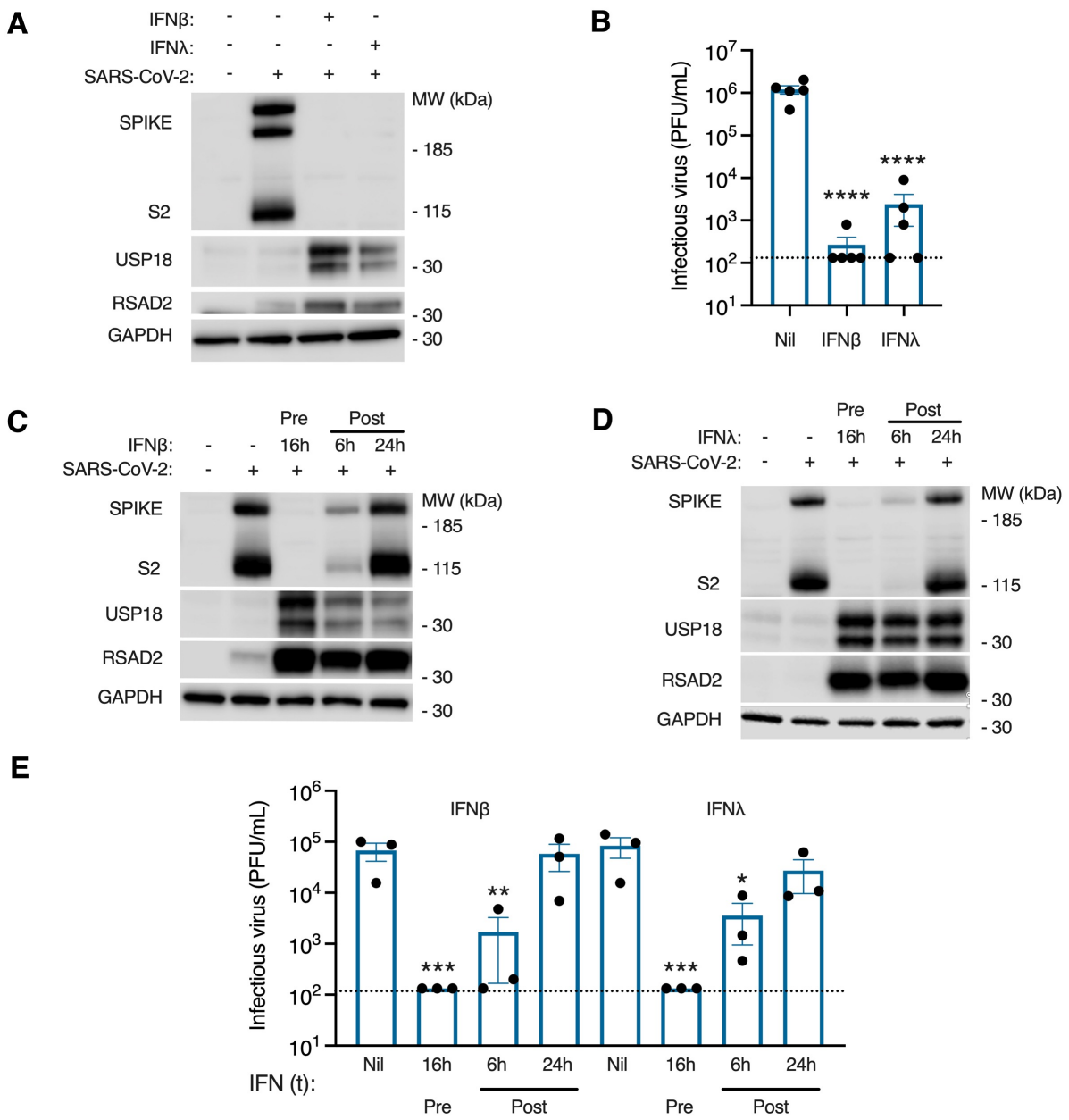

410

411 **Figure 7. Exogenous IFN-I/III treatment controls SARS-CoV-2 replication.** Nasal ALI cultures were pre-
412 treated for 16 h with IFNβ (1000 IU/mL) or IFNλ1 (100 ng/mL) prior to infection (MOI 0.01). (A)
413 Immunoblot of whole-cell lysates prepared from nasal ALI cultures at 48 hpi (representative of
414 experiments in n=4 donors). (B) Plaque assay of apical washes showing significant reduction in
415 infectious particle release at 48 hpi if pre-treated with IFNβ (1000 IU/mL) or IFNλ1 (100 ng/mL) (same
416 experimental conditions as A; n=5 donors, mean ± SEM; **** $P < 0.0001$, ANOVA with Dunnett's post-
417 test correction compared to untreated control). (C-D) Immunoblot of whole-cell lysates prepared at
418 48 hpi. Nasal ALI cultures were either pre-treated with IFNβ (1000 IU/mL, C) or IFNλ1 (100 ng/mL, D)

419 for 16h prior to infection with SARS-CoV-2 or IFN treatment was applied at 6 or 24 hpi. Results
420 representative of experiments in n=3 donors. (E) Plaque assay on apical washes collected at 48 hpi
421 from experiments in C-D (n=3 donors, mean ± SEM; * $P < 0.05$, ** $P < 0.01$, *** $P < 0.001$, ANOVA with
422 Dunnett's post-test correction compared to untreated control). Dotted line indicates lower limit of
423 assay detection.
424

425 **DISCUSSION**

426 We report the most comprehensive characterisation of the human nasal epithelial response to
427 experimental SARS-CoV-2 infection to date, revealing a response dominated at later stages by IFN-
428 I/IIIs and their downstream ISG products. This response partially contained SARS-CoV-2 at later times
429 post-infection, while recombinant IFN-I/III treatment potently blocked SARS-CoV-2 replication,
430 suggesting that mucosal delivery of IFNs could be a promising strategy for post-exposure prophylaxis.
431 The nasal mucosa is likely to be a main point of entry of SARS-CoV-2. Prior single-cell transcriptomic
432 studies implied an abundance of target cells in the nasal mucosa and further suggested that they may
433 be poised to mount an antiviral response[10]. Yet few studies to date have characterised SARS-CoV-2
434 replication in primary human differentiated nasal cells[12-14], while we analyse the host-virus interaction
435 comprehensively, at single-cell resolution and utilising proteomics. Our findings indicate that the host
436 response to SARS-CoV-2 in nasal epithelium is dominated by paracrine IFN-I/III signalling, albeit this
437 response is kinetically delayed. These data contrast with initial reports that SARS-CoV-2 did not induce
438 a robust IFN response in airway epithelial cells[26-28], but are consistent with emerging evidence of IFN-
439 I/III induction in nasal swabs from patients with COVID-19[15,42-44] and with more recent findings in lung
440 airway models[36,43,45-47]. Blockade of the endogenous IFN response had an impact on SARS-CoV-2
441 infection at later stages post-infection, once the IFN response was established, underscoring the
442 delayed kinetic but also emphasising its functional relevance. While the impact of endogenous IFN-
443 I/III signalling upon SARS-CoV-2 replication has not to our knowledge been investigated in nasal cell
444 models, our data are consistent with recent findings in some[43,47], but not all epithelial model
445 systems[27,45]. Our experiments with IAV, PIV3 and SeV - viruses which induced the robust early
446 expression of IFN-I/III, in line with previous studies[12,27,37] - confirm that this delay was not due to an
447 intrinsic property of nasal epithelial cells. The expression of IFN evasion proteins[37,48], the sequestration
448 of viral replication machinery within cytosolic vesicles[49], as well as global reductions in host mRNA
449 content[50] and translational shutdown[51-53] induced by SARS-CoV-2 presumably underlie its capacity to
450 subvert early IFN induction in infected cells. Consistent with this, there was evidence of

451 downregulation of immune pathways including TLR signalling in the proteome of infected cells.
452 However, an important question is what molecular patterns are responsible for IFN-I/III induction at
453 later times. Recent evidence implicates MDA5 as a major sensor of SARS-CoV-2 RNA in epithelial
454 cells[45-47], while other findings suggest a contribution from virus-mediated damage occurring after
455 several days of infection[54]. It will be important to address the relative contribution of host damage-
456 associated molecular patterns versus viral pathogen-associated molecular patterns (e.g. defective
457 viral genomes) accumulating during replication.
458 IFN-I/III signalling is plausibly implicated in protection against life-threatening COVID-19[18-20].
459 Consistent with this, circulating immune cells of patients with severe COVID-19 exhibit impaired ISG
460 responses[55-57]. However, whether the local airway IFN response in the early stages of infection has a
461 decisive role in shaping the subsequent clinical outcome of COVID-19 remains to be conclusively
462 determined. A compelling recent scRNA-seq study reported that patients going on to develop severe
463 disease exhibited a muted ISG response in the nasal airway, in contrast to those with milder disease[15],
464 and is supported by independent findings of attenuated nasal ISG induction in patients with
465 autoantibodies to IFN-I[58], who are prone to more severe disease[20]. Additional strands of evidence
466 suggest a potential link between airway IFN-I/III competence and clinical outcome in COVID-19. Age
467 remains the strongest risk factor for poor outcome in COVID-19, and the efficiency of IFN-I/III
468 induction is known to decline with advancing age[59], and appears to be greater in the nasal airways of
469 children than adults infected with SARS-CoV-2[60]. Other relevant environmental influences, such as
470 exposure to cigarette smoke or other viral infections, are also reported to perturb IFN-I/III responses
471 of airway cells in ways that may be relevant to COVID-19 pathogenesis[43,61].
472 The main limitation of our data in this nasal epithelial culture system is that it did not account for
473 professional immune cells present in the nasal mucosa, for example plasmacytoid dendritic cells[62],
474 which are capable of more rapidly mounting an IFN-I/III response to SARS-CoV-2[63], potentially tipping
475 the scales in favour of the host[64]. We studied cells derived from adult donors, however it is possible
476 that nasal cells from paediatric donors, who are naturally less susceptible to severe COVID-19, may

477 behave differently in terms of their reduced permissiveness to SARS-CoV-2 and/or the greater
478 efficiency of their innate IFN response[60,65]. Furthermore, SARS-CoV-2 variants with mutations in the
479 spike gene have emerged worldwide whilst we were undertaking the experiments described here;
480 these variants may impact viral replication and/or host immunity, and should be included in future
481 studies.
482 Nevertheless, our data, employing a variety of complementary methods, indicate that SARS-CoV-2 has
483 a relatively broad tropism for nasal epithelial cells, confirming suggestions from prior scRNA-seq
484 studies[8,10], other *in vitro* studies of primary nasal[14] and tracheobronchial cells[24,36], and importantly
485 recent scRNA-seq studies of nasal samples from COVID-19 patients[15]. We also identify tropism for the
486 rare deuterosomal cell, marked by expression of FOXN4, as recently reported[36,61,66]. Our findings
487 contrast with the results of Hou and colleagues, who reported exclusive tropism of SARS-CoV-2 for
488 ciliated cells in the nasal airway[13]. It is not immediately clear how to reconcile these findings, given
489 that secretory cells express relevant entry receptors[10,13] and have been identified as a major infected
490 cell type in infected patients[66]. Hou and colleagues used a fluorescent reporter virus, the tropism of
491 which might have been slightly narrower than clinical isolates. It is also worth noting that while we
492 show that all cell types contained SARS-CoV-2 protein, there was a significant reduction in the
493 proportion of goblet cells expressing spike protein, and the intensity of spike immunodetection was
494 significantly greater in ciliated and secretory cells than basal or goblet cells. Ciliated cells also
495 contained more virion-like structures per cell. Collectively, this implies that although all cell types are
496 permissive to SARS-CoV-2 entry, there may also be quantitative differences in the overall efficiency of
497 viral replication in different cell types. Hou and colleagues previously hypothesised that post-entry
498 factors such as intrinsic antiviral immunity might dictate permissiveness. As discussed, we found
499 limited evidence to support such a correlation, since while virtually all nasal epithelial cells
500 demonstrated a basal ISG signature - consistent with *ex vivo* nasal biopsy data[10] - this was apparently
501 insufficient to mediate resistance to SARS-CoV-2, at least at the time point analysed. However, it

502 remains possible that cell-type specific differences in the efficiency of induction of the IFN response
503 (for example in basal cells) might contribute to more subtle variation in permissiveness.
504 The differential response of basal cell types to SARS-CoV-2 at 24 hpi identified by our scRNA-seq
505 analysis appears a novel observation. Basal cells are the stem/progenitor cell population of the
506 airway[67]. Recent data indicate an emerging role for these cells as sentinels of the airway inflammatory
507 response[68]. For example, basal cells detect apoptotic cells in the context of viral inflammation[69],
508 retaining memory of prior immune exposure[70]. More generally, stem/progenitor cell types exhibit
509 enhanced intrinsic antiviral immunity[71]. Future studies should consider mechanism(s) governing the
510 seemingly distinct early antiviral response of nasal airway basal cells to SARS-CoV-2, and its functional
511 relevance.
512 Importantly, from a clinical perspective, the observation that IFN-I/III treatment prevented SARS-CoV-
513 2 infection *in vitro* indicates that chemoprophylaxis with IFN-I/III may have therapeutic value. This
514 approach has already been tested in a small clinical trial in China (although the absence of a control
515 group makes it impossible to judge the efficacy of this approach[72]). Immunisation is the most tractable
516 approach for large-scale primary prevention of COVID-19. However, owing to incomplete vaccine
517 coverage, and reduced vaccine effectiveness in immunocompromised populations or against mildly
518 symptomatic or asymptomatic infection, allied to the emergence of variants that may compromise
519 vaccine efficacy, there will likely continue to be a need for targeted chemoprophylactic therapies to
520 prevent transmission in specific circumstances. These include post-exposure prophylaxis of contacts -
521 to avoid the need for self-isolation - as well as pre-exposure prophylaxis for certain high-risk
522 encounters (e.g. in healthcare settings or prior to long-distance travel). Our data suggest that nasal
523 application of IFNβ or IFNλ1 might have an important role to play in this setting and argue for urgent
524 clinical assessment of this approach. In terms of the therapeutic efficacy of mucosally-administered
525 IFNβ in patients with established COVID-19[41], our findings suggest that early administration may be a
526 key factor determining clinical efficacy. Furthermore, studies in animal models indicate that
527 administration of IFNβ or IFNλ1 later in the disease course may have deleterious effects on viral

528 inflammation and/or airway cell regeneration[73-75], suggesting the existence of a relatively narrow
529 therapeutic window of opportunity.
530 In summary, we have shown that SARS-CoV-2 exhibits broad tropism for nasal epithelial cells, but with
531 preferential infection of ciliated and secretory cell types. Nasal cells mount a robust innate antiviral
532 response to SARS-CoV-2 dominated by paracrine IFN-I/III signalling, which is delayed in onset relative
533 to viral replication, but which is nevertheless capable of exerting partial control at later times post-
534 infection. Upon exposure to exogenous IFN-I/III treatment, these cells adopt a profound antiviral
535 state, highlighting a potential clinical role for recombinant IFNβ or IFNλ1 in chemoprophylaxis and/or
536 therapy of COVID-19.
537
538 **METHODS**
539 **Adult nasal airway epithelial cell culture at air-liquid interface (ALI)**
540 Adult primary human nasal airway epithelial cells were derived from excess clinical material obtained
541 during routine nasal surgical procedures[29]. Ethical approval for sample collection was provided
542 (Research Ethics Committee Reference 17/NE/0361) and written approved consent was provided
543 prior to sample collection. Tissue shaved from the superficial surface of the sample was chopped into
544 ~2 mm^2 pieces and added to RPMI-1640 basal medium containing 0.1% protease (Sigma-Aldrich, UK)
545 and incubated overnight with gentle agitation at 4°C. All large pieces of tissue were discarded, and
546 residual protease was neutralized with 5% FCS. The preparation was centrifuged (200 g; 7 min) and
547 the pellet resuspended in PneumaCult-Ex Plus expansion medium (Stemcell Technologies), then
548 seeded onto 25 cm^2 tissue culture flasks pre-coated with 30 µg/mL Type I collagen (PureCol, Advanced
549 BioMatrix). Flasks were incubated in a humidified atmosphere containing 5% CO2 at 37°C, with
550 medium replaced every 48 hours. Cells were trypsinised at 60-80% confluence and cryopreserved for
551 future use. Upon thawing, cells were grown through an additional expansion phase, then transferred
552 in Ex Plus medium onto collagen-coated 6.5 mm polyester transwell membranes with 0.4 µm pore
553 size (Corning) at a density of 150,000 cells/cm^2. When cells were fully confluent, apical medium was

554 removed and basolateral medium was switched to PneumaCult-ALI-S (Stemcell Technologies). Cells
555 were maintained at air-liquid interface until fully differentiated. Barrier integrity of ALI cultures was
556 monitored by measuring trans-epithelial electrical resistance (TEER, EVOM 2, World Precision
557 Instruments). ALI cultures were validated for use in experiments based on microscopic appearance of
558 appropriate ciliated morphology and TEER > 500 Ω*cm^2. The sex and age of donors are included in
559 Table S4.
560
561 **Viruses, cytokines and inhibitors**
562 A clinical isolate of SARS-CoV-2 (BetaCoV/England/2/2020) was obtained from Public Health England
563 (PHE). This was isolated from a patient in January 2020 and thus represents an early strain of SARS-
564 CoV-2, not known to be affected by variants of concern. The initial stock was propagated once in vero
565 E6 cells. The same viral stock was used for all experiments. As SARS-CoV-2 is a Hazard Group 3
566 pathogen (Advisory Committee on Dangerous Pathogens, UK), all infection experiments were
567 performed in a dedicated Containment Level 3 (CL3) facility by trained personnel. Sendai virus (Cantell
568 strain) and parainfluenza virus 3 (PIV3) was obtained from Richard Randall (St Andrew's University).
569 Influenza A virus (A/PR8/1934/H1N1) was propagated and titred on MDCK cells. For nasal ALI
570 infections, apical poles were gently washed once with warm Dulbecco's modified Eagle's medium
571 (DMEM; Gibco, USA) and then infected with 60 µL dilution of virus in DMEM, at a MOI between 2 and
572 0.01 plaque-forming units per cell for 2 hours, when the virus-containing medium was removed.
573 DMEM was used as inoculum for mock infection. Apical washes (in warm phosphate-buffered saline)
574 were collected at different time points and stored at -80°C for plaque assays. Plaque assays were
575 undertaken in vero E6 cells using a 1.2% (w/v) microcrystalline cellulose overlay (Sigma-Aldrich).
576 Cytokines/inhibitors were used at the following concentrations: human recombinant IFNβ1 (1000
577 ng/mL; Avonex, NDC 59627-002-06, Biogen Inc, USA); IFNλ1 (100 ng/mL; 1598-IL-025, R&D Systems,
578 USA); and Ruxolitinib (10 µM; S1378, Calbiochem, USA) alongside the appropriate dilution of DMSO
579 vehicle. Treatment was applied through basolateral poles.

580

581 **Single cell RNA sequencing (scRNA-seq) sample processing**

582 For the droplet-encapsulation scRNA-seq experiments, ALI cultures were washed with PBS and then
583 incubated with 1x Trypsin-EDTA (ThermoFisher Scientific, USA) for 10 min before the cells were diluted
584 with DMEM and counted using a haemocytometer. 20,000 single cells were loaded onto each channel
585 of a Chromium chip before encapsulation on the Chromium Controller (10x Genomics, USA). The
586 single-cell sequencing libraries were generated using the Single Cell 5' V.1, as per the manufacturer's
587 protocol. Libraries were sequenced using NovoSeq 6000 to achieve a minimum depth of 50,000 raw
588 reads per cell. The libraries were sequenced using the following parameters: Read1: 26 cycles, i7: 8
589 cycles, i5: 0 cycles; Read2: 98 cycles to generate 75 bp paired-end reads.

590

591 **Single-cell RNA sequencing (scRNA-seq) data generation and annotation**

592 Sequencing data were demultiplexed and quantified using the Cellranger tool (version 4.0.0, 10x
593 Genomics) and aligned to the combined human (official Cell Ranger reference, GRCh38-2020-A) and
594 SARS-CoV-2 reference transcriptomes (Ensembl reference Sars_cov_2.ASM985889v3). CellBender
595 (version 0.2.0)[76] was applied to the output from Cell Ranger software after alignment to remove
596 background effect from ambient mRNA released during processing. Doublet detection and exclusion
597 was performed using Scrublet (version 0.2.1) with thresholding of cells with a doublet score above
598 two median absolute deviations from the median. Low-quality cells were removed using thresholds
599 of < 200 genes and > 20% mitochondrial content. The analysis was performed using Seurat (version
600 4.0.1). Data were normalised and log-transformed using NormalizeData and the top 2000 variable
601 genes identified using the FindVariableFeatures tool. The first 20 principal components were batch-
602 adjusted using Harmony (by sample ID) and used to generate the nearest-neighbour graph.
603 Dimensionality reduction and embedding was performed using Uniform Manifold Approximation and
604 Projection (UMAP), with the neighbourhood graph clustered using the Leiden algorithm. The Wilcoxon
605 rank sum test ($\log_2$ fold change threshold of 0.25, adjusted P value of 0.05) was used to identify

606 differentially expressed genes between clusters, and these were annotated based on expression of
607 markers from literature. This annotation was validated by comparing to a recently published scRNA-
608 seq dataset from ex vivo primary nasal cells[15]. The Seurat label transfer tool was used to assign
609 predicted identities to our data using the external published data as reference. The robustness of our
610 annotation was then assessed by the strength of its correlation with this prediction.
611
612 **Gene set scoring and gene set enrichment analysis**
613 A published gene set derived from IFN alpha or IFN gamma-treated human nasal basal cells[11] was used
614 to generate a list of epithelial-specific IFN-stimulated genes (ISGs). To calculate basal expression of
615 ISGs within the unexposed cells, over-expression of this gene list was assessed using the Seurat
616 AddModuleScore tool. Differences between clusters was compared by a Wilcoxon rank sum test
617 (adjusted alpha 0.05) with Benjamini-Hochburg multiple test correction applied.
618 Gene set enrichment analysis was performed using the fgsea tool[77]. Genes were ordered between
619 mock-infected and infected cells by fold-change in expression with Wilcoxon rank sum testing using
620 the FindAllMarkers function in Seurat, but without thresholds. Gene sets from Hallmark, Reactome
621 and Biocarta were used as reference after filtering to exclude those with fewer than 50 and greater
622 than 200 genes. Output from fgsea was further filtered to remove pathways that were not significantly
623 enriched in any cell type (adjusted P value <0.05) followed by further manual curation of the resultant
624 pathways.
625
626 **Regulon scoring and analysis**
627 The DoRoTHea/Viper package in R was used to score regulon activity by cell[78]. Human regulons from
628 DoRoTHea were filtered for those with a confidence score A-C. Normalised enrichment scores (NES)
629 for each transcription factor (TF) were calculated using run_viper with a minimum regulon size of 4 on
630 the complete gene expression matrix. To estimate TF activity over baseline within each cell type in the
631 infected cells, the median NES from the mock-infected clusters was subtracted from the equivalent in

632 the infected cluster. These scores were then scaled within each TF to give comparative estimate of TF
633 activity between clusters.
634
635 **Quantitative RT-PCR**
636 Total RNA was isolated using TRIzol™ reagent (Invitrogen, Carlsbad, CA, USA) according to the
637 manufacturer's instructions. For qPCR analyses of transcripts, 250 ng of RNA isolated from the nasal
638 epithelial cells was reverse transcribed with Superscript III (ThermoFisher Scientific), and the resulting
639 cDNA templates were subjected to qPCR with a TaqMan™ Gene Expression Master Mix (Applied
640 Biosystems, MA, USA) and AriaMx real-time PCR system (Agilent Technologies, CA, USA) according to
641 the manufacturer's instructions. The following TaqMan gene expression assays (Thermo Fischer) were
642 used: *IFNA1* (Hs03044218_g1), *TNF* (Hs00174128_m1). The primers were designed using the Roche
643 Universal Probe Library (UPL) Assay Design tool (Roche, Basel, Switzerland) with the indicated UPL
644 probes. All other primer and probe information is described in Table S5. Cycling conditions were as
645 follows: reverse transcription at 50°C for 15 min, followed by initial polymerase activation at 95°C for
646 10 min, then 40 cycles of denaturation at 95°C for 15 sec and annealing/extension at 60°C for 1 min.
647 The $2^{-\Delta\Delta Ct}$ method was used to calculate the relative expression of genes. Each sample was run in
648 duplicate. Samples were normalised to the endogenous housekeeping gene expression, either
649 *RNASEP* for *N* gene expression, or *18S* for all other genes.
650
651 **Immunofluorescence**
652 Immunofluorescence analysis was performed in accordance with published methods[79]. Infected and
653 mock-infected membranes were fixed *in situ* with 4% (w/v) paraformaldehyde overnight at 4°C, before
654 removal from transwells and sectioning. Membranes were washed twice for 5 min in PBS plus 0.1%
655 (v/v) Triton X-100 (Sigma-Aldrich) before being blocked with a 1% (w/v) BSA solution in PBS with 0.5%
656 (v/v) Tween 20 (Sigma-Aldrich; PBST) for one hour at room temperature (RT). Membranes were
657 incubated with primary antibodies for 2 hours at RT. Antibodies used are listed in Table S6.

658 Membranes were washed three times for 5 min in PBST before incubation with appropriate
659 fluorescence-conjugated secondary antibodies for 2 hours at RT. This process was repeated as part of
660 a sequential staining process where required. Membranes were washed three times for 5 min in PBST
661 before being incubated with DAPI (50 nM; Sigma-Aldrich) as a nuclear counterstain, and phalloidin,
662 DyLight 650 (1 unit/mL; ThermoFisher) where required, for 10 min. Membranes were then mounted
663 in MOWIOL mounting media (Sigma-Aldrich) and coverslips applied. Appropriate secondary only
664 controls were performed as required. Images were captured using a Nikon A1 confocal microscope
665 (Nikon, Japan), with all capture settings standardised. For analysis three random fields per sample
666 were captured at x20 magnification and analysed via Fiji (Version 2.0) using the Cell Counter plugin.
667 Total cell count, and number of spike protein-positive cells, were determined by segmenting images
668 using ZO-1 and DAPI to identify individual cells. Mean pixel intensity of the spike protein in positive
669 cells was also determined using the Plot Profile plugin.
670
671 **Immunoblot**
672 Immunoblotting was carried out as previously described[40]. Briefly, proteins from cell lysates were
673 separated by 10% sodium dodecyl sulphate polyacrylamide gel electrophoresis (SDS-PAGE) using
674 MOPS running buffer (Thermo Fisher, USA), and transferred to a nitrocellulose membrane (Millipore,
675 USA) using NuPage Tris-Bis Transfer Buffer (Thermo Fisher) for immunoblotting (for details of
676 antibodies see Table S6). Blots were developed with Pierce ECL Western blotting substrate (Thermo
677 Fisher) and imaged on a LI-COR Odyssey Fc (LI-COR, USA). Densitometry was undertaken using
678 ImageStudio software (LI-COR).
679
680 **Transmission electron microscopy (TEM)**
681 Cultures were fixed with 2% glutaraldehyde (Sigma-Aldrich, MO, USA) in 0.1 M sodium cacodylate (pH
682 7.4) buffer in the apical and basal compartment and then kept at 4°C overnight. For TEM resin
683 processing, the monolayer membranes were removed from the insert frame and placed in microwave

684 sample holders. The Pelco Biowave Pro+ microwave (Pelco, CA, USA), incorporating the Pelco ColdSpot
685 Pro system, was used for the following steps of the processing. The ColdSpot system
686 improves inconsistent wattage supply to the microwave compartment, therefore protecting samples
687 from excess microwave energy. The range temperature was set at 23−27°C. Following buffer rinses
688 (three pulses at 150 watts (W) for 40 secs) the samples were post-fixed in 1% osmium tetroxide for 8
689 min [pulse microwaved (MW), 100 W] and rinsed in distilled H_2O (three times at 150 W for 40 secs,
690 per step). Samples were dehydrated in a graded series of acetone (25%; 50%; 75%; three times with
691 100% (v/v); 150 W, 40 secs per step) before being impregnated with increasing concentrations of
692 epoxy resin (medium resin; TAAB, UK) in acetone (25%; 50%; 75%; three times at 100% (v/v); 300 W,
693 3 min per step). The samples were then embedded in 100% fresh resin and left to polymerise at 60°C
694 in a conventional oven for a minimum of 24 hours. All resin blocks were trimmed using a razor blade
695 to form a trapezoid block face. Sections were cut on an ultramicrotome using a diamond knife. Semi
696 thin sections (0.5 µm) were stained with toluidine blue and viewed on a light microscope to verify
697 presence of cell monolayers. Ultrathin sections (70 nm) were then cut and picked up onto pioloform-
698 coated copper grids. Grids were stained with 1% (w/v) uranyl acetate (30 min) and 3% (w/v) lead
699 citrate (7 min) to improve contrast. All sections were examined using a HT7800 120 kV TEM (Hitachi,
700 Japan). Digital micrographs were captured using an EMSIS Xarosa CMOS Camera with Radius software
701 (EMSIS, Germany). ImageJ software (Version 2.0) was used to enhance the contrast by increasing the
702 percentage of saturated pixels to 1% to aid virus-like particle identification. Virus-like particles
703 (~70 nm in diameter) were counted using the cell counter plugin in at least 6 goblet cells and 16
704 ciliated cells per donor. Data were presented as number of virus-like particles per cell.
705
706 **Proteome sample preparation**
707 The protein concentration was determined by EZQ® protein quantification assay. Protein digestion was
708 performed using the S-Trap™ sample preparation method and TMT-16 plex labelling was carried out
709 as per the manufacturer's instructions. Samples were cleaned using MacroSpin columns, and dried

710 down prior to offline high-performance liquid chromatography fractionation. Peptides were
711 fractionated on a Basic Reverse Phase column on a Dionex Ultimate 3000 off-line LC system. A total of
712 18 fractions were collected, and each fraction was acidified and dried. Peptides were dissolved in 5%
713 formic acid, and each sample was independently analysed on an Orbitrap Fusion Lumos Tribrid mass
714 spectrometer, connected to an UltiMate 3000 RSLCnano System. All spectra were analysed using
715 MaxQuant 1.6.10.43 and searched against SwissProt *Homo sapiens* and Trembl SARS-CoV-2 FASTA
716 files. Reporter ion MS3 was used for quantification and the additional parameter of quantitation labels
717 with 16 plex TMT on N-terminus or lysine was included. A protein and peptide false discovery rate
718 (FDR) of less than 1% was employed in MaxQuant. Moderated t-tests, with patient accounted for in
719 the linear model, was performed using Limma, where proteins with an adjusted $P < 0.05$ were
720 considered as statistically significant. All analysis was performed using R. Raw data are present in
721 supplementary dataset 5. A comprehensive description of the methods can be found in the
722 supplementary methods.
723
724 **Statistical analysis**
725 Statistical analysis was performed and figures assembled using GraphPad Prism V9 (GraphPad
726 Software, USA). Data are presented as mean ± SEM of individual donor values (derived typically from
727 2-3 independent repeat experiments per donor). The donor was used as the unit of experiment for
728 statistical analysis purposes. Continuous data were normalised or log-transformed prior to analysis
729 using parametric significance tests, or if this was not possible, were analysed using nonparametric
730 significance tests. Differences between two groups were compared using an unpaired, two-tailed
731 Student's t-test (or Mann-Whitney test for TEM image analysis), whereas differences between more
732 than two groups used ANOVA, with Dunnett's post-test correction for multiple comparisons when
733 comparing to a single reference point (e.g. mock-infected or time zero) or with Sidak's post-test
734 correction for other multiple comparisons (e.g. between differently treated donors at the same time
735 point). In some cases, data were normalised to a reference point, where a one-sample t-test was used.

736 Unless stated otherwise, a two-tailed alpha of < 0.05 was the threshold for statistical significance.
737 Statistical analysis of proteomics and transcriptomics data sets is described in the relevant sections
738 above.
739
740 **Data availability**
741 Source data are provided with this paper. This includes uncropped blots, all quantitative data and the
742 results of differential expression analysis of RNA-seq and proteomics data, which are included as
743 supplementary datasets. Additional raw data are available on request from the corresponding author
744 providing ethical approvals permit sharing of data. The mass spectrometry proteomics data have been
745 deposited to the ProteomeXchange Consortium[80] via the PRIDE partner repository[81] with the dataset
746 identifier PXD022523. This can be accessed through the Username: reviewer_pxd022523@ebi.ac.uk
747 and the Password: UaEXYFKF. Raw RNA sequencing data have been deposited to the European
748 Genome-Phenome Archive (accession pending). Processed scRNAseq data is available at Zenodo
749 (https://zenodo.org/record/4564332).
750
751 **Code availability**
752 Analysis scripts and codes are available at github.com/haniffalab/covid_nasal_epithelium.
753
754 **Acknowledgements**
755 We acknowledge Public Health England for providing the SARS-CoV-2 isolate and Professor R Randall
756 (St Andrew's University) for providing Sendai and parainfluenza 3 viruses and the vero E6 cell line. We
757 thank M Glanville and Dr S Dainty (Newcastle University Infectious Disease Facility) and Dr A Laude
758 (Bioimaging facility) for assistance. Tissue for this study was provided by the Newcastle Biobank which
759 is supported by the Newcastle upon Tyne NHS Foundation Trust and Newcastle University. The work
760 was part-funded by the Barbour Foundation (CJAD, SH, MB, MT, MH, CW), the UK-Coronavirus
761 Immunology Consortium (CJAD, SH, MH) and the Medical Research Council SHIELD antimicrobial

resistance consortium (JS, AJS). CFH is supported by a Medical Research Council studentship (MR/NO13840/1) and MB by an MRC Clinician Scientist Fellowship (MR/M008797/1). MT and SH are funded by Wellcome Investigator Awards (215542/Z/19/Z and 207556/Z/17/Z). CJAD and GR are Wellcome Clinical Research Career Development Fellows (211153/Z/18/Z and 214539/Z/18/Z). MED is a Marie Sklodowska Curie Fellow within the European Union's Horizon 2020 research and innovation programme under the Marie Sklodowska-Curie grant agreement No. 890296. MH is funded by Wellcome (WT107931/Z/15/Z), The Lister Institute for Preventive Medicine and Newcastle NIHR Biomedical Research Centre (BRC). JPG, CW and BV were supported by the Medical Research Foundation (MRF Respiratory Diseases Research Award to JPG; Grant MRF-091-0001-RGGARNE) and Boehringer Ingelheim. TEM work was supported by a BBSRC Alert17 grant (BB/R013942/1). AJS is a National Institute for Health Research (NIHR) Senior Investigator. The views expressed in this article are those of the author(s) and not necessarily those of the NIHR, or the Department of Health and Social Care. The funders had no role in the study design, data collection and analysis, decision to publish, or preparation of the manuscript.

Author contributions

Conceived the study: MB, CW, CJAD with MH, SH, MT. Experimental design: MH, SH, MB, CW, MT, GR, CJAD. Nasal model development and patient material: IJH, BV, JS, JPG, SC, JP, AJS, MB, CW. Virology data generation, analysis and interpretation: CFH, BJT, JSS, FG, AIG, AK, LH, TD, SH, CJAD. Proteomics data generation, analysis and interpretation: MED, SM, MT. Single-cell sequencing data generation, analysis and interpretation: RAB, ES, RH, JC, MH, GR. Supervised research: AJS, MH, SH, MB, CW, MT, GR, CJAD. Drafted the manuscript: CFH and CJAD with ES, BV, MED, TD, MT, GR. Revised the manuscript: RAB, MED, IJH, JSS, AJS, MH, SH, CW. Approved the manuscript for submission: all authors.

Declaration of competing interests

788 SH declares honoraria from CSL Behring and Takeda for teaching and consultancy. The remaining
789 authors declare no financial or non-financial competing interests.

790 **References**

791 1 Zhu, N. *et al.* A Novel Coronavirus from Patients with Pneumonia in China, 2019. *N*
792 *Engl J Med* **382**, 727-733, doi:10.1056/NEJMoa2001017 (2020).
793 2 Hoffmann, M. *et al.* SARS-CoV-2 Cell Entry Depends on ACE2 and TMPRSS2 and Is
794 Blocked by a Clinically Proven Protease Inhibitor. *Cell* **181**, 271-280 e278,
795 doi:10.1016/j.cell.2020.02.052 (2020).
796 3 Huang, C. *et al.* Clinical features of patients infected with 2019 novel coronavirus in
797 Wuhan, China. *Lancet* **395**, 497-506, doi:10.1016/S0140-6736(20)30183-5 (2020).
798 4 Knight, S. R. *et al.* Risk stratification of patients admitted to hospital with covid-19
799 using the ISARIC WHO Clinical Characterisation Protocol: development and validation
800 of the 4C Mortality Score. *BMJ* **370**, m3339, doi:10.1136/bmj.m3339 (2020).
801 5 Group, R. C. *et al.* Dexamethasone in Hospitalized Patients with Covid-19 - Preliminary
802 Report. *N Engl J Med*, doi:10.1056/NEJMoa2021436 (2020).
803 6 Group, R. C. Tocilizumab in patients admitted to hospital with COVID-19 (RECOVERY):
804 a randomised, controlled, open-label, platform trial. *Lancet* **397**, 1637-1645,
805 doi:10.1016/S0140-6736(21)00676-0 (2021).
806 7 Cevik, M., Kuppalli, K., Kindrachuk, J. & Peiris, M. Virology, transmission, and
807 pathogenesis of SARS-CoV-2. *BMJ* **371**, m3862, doi:10.1136/bmj.m3862 (2020).
808 8 Chen, M. *et al.* Elevated ACE-2 expression in the olfactory neuroepithelium:
809 implications for anosmia and upper respiratory SARS-CoV-2 entry and replication. *Eur*
810 *Respir J* **56**, doi:10.1183/13993003.01948-2020 (2020).
811 9 Hoagland, D. A. *et al.* Leveraging the antiviral type I interferon system as a first line of
812 defense against SARS-CoV-2 pathogenicity. *Immunity*,
813 doi:10.1016/j.immuni.2021.01.017 (2021).
814 10 Sungnak, W. *et al.* SARS-CoV-2 entry factors are highly expressed in nasal epithelial
815 cells together with innate immune genes. *Nat Med* **26**, 681-687, doi:10.1038/s41591-
816 020-0868-6 (2020).
817 11 Ziegler, C. G. K. *et al.* SARS-CoV-2 Receptor ACE2 Is an Interferon-Stimulated Gene in
818 Human Airway Epithelial Cells and Is Detected in Specific Cell Subsets across Tissues.
819 *Cell* **181**, 1016-1035 e1019, doi:10.1016/j.cell.2020.04.035 (2020).
820 12 Gamage, A. M. *et al.* Infection of human Nasal Epithelial Cells with SARS-CoV-2 and a
821 382-nt deletion isolate lacking ORF8 reveals similar viral kinetics and host
822 transcriptional profiles. *PLoS Pathog* **16**, e1009130,
823 doi:10.1371/journal.ppat.1009130 (2020).
824 13 Hou, Y. J. *et al.* SARS-CoV-2 Reverse Genetics Reveals a Variable Infection Gradient in
825 the Respiratory Tract. *Cell* **182**, 429-446 e414, doi:10.1016/j.cell.2020.05.042 (2020).
826 14 Pizzorno, A. *et al.* Characterization and Treatment of SARS-CoV-2 in Nasal and
827 Bronchial Human Airway Epithelia. *Cell Rep Med* **1**, 100059,
828 doi:10.1016/j.xcrm.2020.100059 (2020).
829 15 Ziegler, C. G. K. *et al.* Impaired local intrinsic immunity to SARS-CoV-2 infection in
830 severe COVID-19. *Cell*, doi:10.1016/j.cell.2021.07.023 (2021).
831 16 Onabajo, O. O. *et al.* Interferons and viruses induce a novel truncated ACE2 isoform
832 and not the full-length SARS-CoV-2 receptor. *Nat Genet* **52**, 1283-1293,
833 doi:10.1038/s41588-020-00731-9 (2020).

17 Duncan, C. J. A., Randall, R. E. & Hambleton, S. Genetic Lesions of Type I Interferon Signalling in Human Antiviral Immunity. *Trends Genet* **37**, 46-58, doi:10.1016/j.tig.2020.08.017 (2021).
18 Zhang, Q. *et al.* Inborn errors of type I IFN immunity in patients with life-threatening COVID-19. *Science* **370**, doi:10.1126/science.abd4570 (2020).
19 Pairo-Castineira, E. *et al.* Genetic mechanisms of critical illness in Covid-19. *Nature*, doi:10.1038/s41586-020-03065-y (2020).
20 Bastard, P. *et al.* Autoantibodies against type I IFNs in patients with life-threatening COVID-19. *Science* **370**, doi:10.1126/science.abd4585 (2020).
21 Lokugamage, K. G. *et al.* Type I Interferon Susceptibility Distinguishes SARS-CoV-2 from SARS-CoV. *J Virol* **94**, doi:10.1128/JVI.01410-20 (2020).
22 Felgenhauer, U. *et al.* Inhibition of SARS-CoV-2 by type I and type III interferons. *J Biol Chem* **295**, 13958-13964, doi:10.1074/jbc.AC120.013788 (2020).
23 Lee, J. S. & Shin, E. C. The type I interferon response in COVID-19: implications for treatment. *Nat Rev Immunol* **20**, 585-586, doi:10.1038/s41577-020-00429-3 (2020).
24 Zhu, N. *et al.* Morphogenesis and cytopathic effect of SARS-CoV-2 infection in human airway epithelial cells. *Nat Commun* **11**, 3910, doi:10.1038/s41467-020-17796-z (2020).
25 Fiege, J. K. *et al.* Single cell resolution of SARS-CoV-2 tropism, antiviral responses, and susceptibility to therapies in primary human airway epithelium. *PLoS Pathog* **17**, e1009292, doi:10.1371/journal.ppat.1009292 (2021).
26 Vanderheiden, A. *et al.* Type I and Type III Interferons Restrict SARS-CoV-2 Infection of Human Airway Epithelial Cultures. *J Virol* **94**, doi:10.1128/JVI.00985-20 (2020).
27 Blanco-Melo, D. *et al.* Imbalanced Host Response to SARS-CoV-2 Drives Development of COVID-19. *Cell* **181**, 1036-1045 e1039, doi:10.1016/j.cell.2020.04.026 (2020).
28 Huang, J. *et al.* SARS-CoV-2 Infection of Pluripotent Stem Cell-derived Human Lung Alveolar Type 2 Cells Elicits a Rapid Epithelial-Intrinsic Inflammatory Response. *bioRxiv*, doi:10.1101/2020.06.30.175695 (2020).
29 Mavin, E. *et al.* Real-time measurement of cellular bioenergetics in fully differentiated human nasal epithelial cells grown at air-liquid-interface. *Am J Physiol Lung Cell Mol Physiol* **318**, L1158-L1164, doi:10.1152/ajplung.00414.2019 (2020).
30 Vieira Braga, F. A. *et al.* A cellular census of human lungs identifies novel cell states in health and in asthma. *Nat Med* **25**, 1153-1163, doi:10.1038/s41591-019-0468-5 (2019).
31 Ruiz Garcia, S. *et al.* Novel dynamics of human mucociliary differentiation revealed by single-cell RNA sequencing of nasal epithelial cultures. *Development* **146**, doi:10.1242/dev.177428 (2019).
32 Xiu, S. *et al.* Inhibitors of SARS-CoV-2 Entry: Current and Future Opportunities. *J Med Chem* **63**, 12256-12274, doi:10.1021/acs.jmedchem.0c00502 (2020).
33 Prelli Bozzo, C. *et al.* IFITM proteins promote SARS-CoV-2 infection and are targets for virus inhibition in vitro. *Nat Commun* **12**, 4584, doi:10.1038/s41467-021-24817-y (2021).
34 Li, S. *et al.* Metabolic reprogramming and epigenetic changes of vital organs in SARS-CoV-2-induced systemic toxicity. *JCI Insight* **6**, doi:10.1172/jci.insight.145027 (2021).
35 Moolamalla, S. T. R., Balasubramanian, R., Chauhan, R., Priyakumar, U. D. & Vinod, P. K. Host metabolic reprogramming in response to SARS-CoV-2 infection: A systems

880 biology approach. *Microb Pathog* **158**, 105114, doi:10.1016/j.micpath.2021.105114
881 (2021).
882 36 Ravindra, N. G. *et al.* Single-cell longitudinal analysis of SARS-CoV-2 infection in human
883 airway epithelium identifies target cells, alterations in gene expression, and cell state
884 changes. *PLoS Biol* **19**, e3001143, doi:10.1371/journal.pbio.3001143 (2021).
885 37 Lei, X. *et al.* Activation and evasion of type I interferon responses by SARS-CoV-2. *Nat*
886 *Commun* **11**, 3810, doi:10.1038/s41467-020-17665-9 (2020).
887 38 Cardoso, R. S. *et al.* Host Retromer Protein Sorting Nexin 2 Interacts with Human
888 Respiratory Syncytial Virus Structural Proteins and is Required for Efficient Viral
889 Production. *mBio* **11**, doi:10.1128/mBio.01869-20 (2020).
890 39 Bergant Marusic, M., Ozbun, M. A., Campos, S. K., Myers, M. P. & Banks, L. Human
891 papillomavirus L2 facilitates viral escape from late endosomes via sorting nexin 17.
892 *Traffic* **13**, 455-467, doi:10.1111/j.1600-0854.2011.01320.x (2012).
893 40 Duncan, C. J. A. *et al.* Severe type I interferonopathy and unrestrained interferon
894 signaling due to a homozygous germline mutation in STAT2. *Sci Immunol* **4**,
895 doi:10.1126/sciimmunol.aav7501 (2019).
896 41 Monk, P. D. *et al.* Safety and efficacy of inhaled nebulised interferon beta-1a (SNG001)
897 for treatment of SARS-CoV-2 infection: a randomised, double-blind, placebo-
898 controlled, phase 2 trial. *Lancet Respir Med*, doi:10.1016/S2213-2600(20)30511-7
899 (2020).
900 42 Antonelli, G. *et al.* Type I interferons can be detected in respiratory swabs from SARS-
901 Cov-2 infected patients. *J Clin Virol* **128**, 104450, doi:10.1016/j.jcv.2020.104450
902 (2020).
903 43 Cheemarla, N. R. *et al.* Dynamic innate immune response determines susceptibility to
904 SARS-CoV-2 infection and early replication kinetics. *J Exp Med* **218**,
905 doi:10.1084/jem.20210583 (2021).
906 44 Mick, E. *et al.* Upper airway gene expression reveals suppressed immune responses to
907 SARS-CoV-2 compared with other respiratory viruses. *Nat Commun* **11**, 5854,
908 doi:10.1038/s41467-020-19587-y (2020).
909 45 Rebendenne, A. *et al.* SARS-CoV-2 triggers an MDA-5-dependent interferon response
910 which is unable to control replication in lung epithelial cells. *J Virol*,
911 doi:10.1128/JVI.02415-20 (2021).
912 46 Sampaio, N. G. *et al.* The RNA sensor MDA5 detects SARS-CoV-2 infection. *Sci Rep* **11**,
913 13638, doi:10.1038/s41598-021-92940-3 (2021).
914 47 Yin, X. *et al.* MDA5 Governs the Innate Immune Response to SARS-CoV-2 in Lung
915 Epithelial Cells. *Cell Rep* **34**, 108628, doi:10.1016/j.celrep.2020.108628 (2021).
916 48 Kumar, A. *et al.* SARS-CoV-2 Nonstructural Protein 1 Inhibits the Interferon Response
917 by Causing Depletion of Key Host Signaling Factors. *J Virol* **95**, e0026621,
918 doi:10.1128/JVI.00266-21 (2021).
919 49 Wolff, G., Melia, C. E., Snijder, E. J. & Barcena, M. Double-Membrane Vesicles as
920 Platforms for Viral Replication. *Trends Microbiol* **28**, 1022-1033,
921 doi:10.1016/j.tim.2020.05.009 (2020).
922 50 Finkel, Y. *et al.* SARS-CoV-2 uses a multipronged strategy to impede host protein
923 synthesis. *Nature* **594**, 240-245, doi:10.1038/s41586-021-03610-3 (2021).
924 51 Schubert, K. *et al.* SARS-CoV-2 Nsp1 binds the ribosomal mRNA channel to inhibit
925 translation. *Nat Struct Mol Biol* **27**, 959-966, doi:10.1038/s41594-020-0511-8 (2020).

926 52 Thoms, M. *et al.* Structural basis for translational shutdown and immune evasion by
927 the Nsp1 protein of SARS-CoV-2. *Science* **369**, 1249-1255,
928 doi:10.1126/science.abc8665 (2020).
929 53 Hsu, J. C., Laurent-Rolle, M., Pawlak, J. B., Wilen, C. B. & Cresswell, P. Translational
930 shutdown and evasion of the innate immune response by SARS-CoV-2 NSP14 protein.
931 *Proc Natl Acad Sci U S A* **118**, doi:10.1073/pnas.2101161118 (2021).
932 54 Robinot, R. *et al.* SARS-CoV-2 infection induces the dedifferentiation of multiciliated
933 cells and impairs mucociliary clearance. *Nat Commun* **12**, 4354, doi:10.1038/s41467-
934 021-24521-x (2021).
935 55 Galani, I. E. *et al.* Untuned antiviral immunity in COVID-19 revealed by temporal type
936 I/III interferon patterns and flu comparison. *Nat Immunol* **22**, 32-40,
937 doi:10.1038/s41590-020-00840-x (2021).
938 56 Hadjadj, J. *et al.* Impaired type I interferon activity and inflammatory responses in
939 severe COVID-19 patients. *Science* **369**, 718-724, doi:10.1126/science.abc6027 (2020).
940 57 Stephenson, E. *et al.* Single-cell multi-omics analysis of the immune response in
941 COVID-19. *Nat Med* **27**, 904-916, doi:10.1038/s41591-021-01329-2 (2021).
942 58 Lopez, J. *et al.* Early nasal type I IFN immunity against SARS-CoV-2 is compromised in
943 patients with autoantibodies against type I IFNs. *J Exp Med* **218**,
944 doi:10.1084/jem.20211211 (2021).
945 59 Molony, R. D. *et al.* Aging impairs both primary and secondary RIG-I signaling for
946 interferon induction in human monocytes. *Sci Signal* **10**,
947 doi:10.1126/scisignal.aan2392 (2017).
948 60 Loske, J. *et al.* Pre-activated antiviral innate immunity in the upper airways controls
949 early SARS-CoV-2 infection in children. *Nat Biotechnol*, doi:10.1038/s41587-021-
950 01037-9 (2021).
951 61 Purkayastha, A. *et al.* Direct Exposure to SARS-CoV-2 and Cigarette Smoke Increases
952 Infection Severity and Alters the Stem Cell-Derived Airway Repair Response. *Cell Stem*
953 *Cell* **27**, 869-875 e864, doi:10.1016/j.stem.2020.11.010 (2020).
954 62 Hartmann, E. *et al.* Analysis of plasmacytoid and myeloid dendritic cells in nasal
955 epithelium. *Clin Vaccine Immunol* **13**, 1278-1286, doi:10.1128/CVI.00172-06 (2006).
956 63 Onodi, F. *et al.* SARS-CoV-2 induces human plasmacytoid pre-dendritic cell
957 diversification via UNC93B and IRAK4. *bioRxiv*, doi:10.1101/2020.07.10.197343
958 (2021).
959 64 Cervantes-Barragan, L. *et al.* Plasmacytoid dendritic cells produce type I interferon and
960 reduce viral replication in airway epithelial cells after SARS-CoV-2 infection. *bioRxiv*,
961 doi:10.1101/2021.05.12.443948 (2021).
962 65 Pierce, C. A. *et al.* Natural mucosal barriers and COVID-19 in children. *JCI Insight* **6**,
963 doi:10.1172/jci.insight.148694 (2021).
964 66 Ziegler, C. G. K. *et al.* Impaired local intrinsic immunity to SARS-CoV-2 infection in
965 severe COVID-19. *bioRxiv*, doi:10.1101/2021.02.20.431155 (2021).
966 67 Rock, J. R. *et al.* Basal cells as stem cells of the mouse trachea and human airway
967 epithelium. *Proc Natl Acad Sci U S A* **106**, 12771-12775, doi:10.1073/pnas.0906850106
968 (2009).
969 68 Hewitt, R. J. & Lloyd, C. M. Regulation of immune responses by the airway epithelial
970 cell landscape. *Nat Rev Immunol* **21**, 347-362, doi:10.1038/s41577-020-00477-9
971 (2021).

69 Fujino, N. *et al.* Sensing of apoptotic cells through Axl causes lung basal cell proliferation in inflammatory diseases. *J Exp Med* **216**, 2184-2201, doi:10.1084/jem.20171978 (2019).

70 Ordovas-Montanes, J. *et al.* Allergic inflammatory memory in human respiratory epithelial progenitor cells. *Nature* **560**, 649-654, doi:10.1038/s41586-018-0449-8 (2018).

71 Wu, X. *et al.* Intrinsic Immunity Shapes Viral Resistance of Stem Cells. *Cell* **172**, 423-438 e425, doi:10.1016/j.cell.2017.11.018 (2018).

72 Meng, Z. *et al.* An experimental trial of recombinant human interferon alpha nasal drops to prevent COVID-19 in medical staff in an epidemic area. *MedRxiv*, doi:doi.org/10.1101/2020.04.11.20061473 (2020).

73 Boudewijns, R. *et al.* STAT2 signaling restricts viral dissemination but drives severe pneumonia in SARS-CoV-2 infected hamsters. *Nat Commun* **11**, 5838, doi:10.1038/s41467-020-19684-y (2020).

74 Major, J. *et al.* Type I and III interferons disrupt lung epithelial repair during recovery from viral infection. *Science* **369**, 712-717, doi:10.1126/science.abc2061 (2020).

75 Broggi, A. *et al.* Type III interferons disrupt the lung epithelial barrier upon viral recognition. *Science* **369**, 706-712, doi:10.1126/science.abc3545 (2020).

76 Fleming, S. J., Marioni, J. C. & Babadi, M. CellBender remove-background: a deep generative model for unsupervised removal of background noise from scRNA-seq datasets. *bioRxiv*, doi:10.1101/791699 (2019).

77 Korotkevich, G. *et al.* Fast gene set enrichment analysis. *bioRxiv*, doi:10.1101/060012 (2021).

78 Holland, C. H. *et al.* Robustness and applicability of transcription factor and pathway analysis tools on single-cell RNA-seq data. *Genome Biol* **21**, 36, doi:10.1186/s13059-020-1949-z (2020).

79 Crowe, A. R. & Yue, W. Semi-quantitative Determination of Protein Expression using Immunohistochemistry Staining and Analysis: An Integrated Protocol. *Bio Protoc* **9**, doi:10.21769/BioProtoc.3465 (2019).

80 Deutsch, E. W. *et al.* The ProteomeXchange consortium in 2017: supporting the cultural change in proteomics public data deposition. *Nucleic Acids Res* **45**, D1100-D1106, doi:10.1093/nar/gkw936 (2017).

81 Perez-Riverol, Y. *et al.* The PRIDE database and related tools and resources in 2019: improving support for quantification data. *Nucleic Acids Res* **47**, D442-D450, doi:10.1093/nar/gky1106 (2019).